Science

Detection and Characterization of Rocks and Rock Size-Frequency Distributions at the Final Four Mars Science Laboratory Landing Sites

M. Golombek[1], A. Huertas[1], D. Kipp[1], F. Calef[1]

[1]Jet Propulsion Laboratory, California Institute of Technology, Pasadena, CA 91109, USA, mgolombek@jpl.nasa.gov

Abstract

Background: Shadows cast from rocks in High-Resolution Imaging Science Experiment (HiRISE) images were used during Phoenix landing site selection to measure the diameter and height of rocks in the northern plains using an automated rock detector algorithm that fits ellipses to the shadows and cylinders to the rocks. Results show that the size-frequency distribution of rocks >1.5 m diameter are fully resolvable in HiRISE images and follow the same exponential models developed from lander measurements of smaller rocks distributions at the landing sites.

Method: Greater image complexity at prospective Mars Science landing sites required improvements in shadow segmentation, which included 4 blind deconvolution steps to sharpen the rock shadows and sectional image processing. Shadows of non-rocks were removed by fitting model size-frequency distributions to rocks 1.5-2.25 m diameter in 450 m bins, all of which significantly improved the rock detection algorithm.

Conclusion: Rock distributions measured from orbit and the ground for the Phoenix landing site follow the same exponential model size-frequency distribution (within 1% rock abundance), further validating accurate extrapolations of rock abundance using HiRISE images. Size-frequency distributions determined in 450 m HiRISE bins matched model distributions and indicates average rock abundances of 5.4±2.6%, 3.9±3.0%, 0.3±1.1% and 3.3±2.7% at the Mars Science Laboratory (MSL) Eberswalde, Gale, Holden and Mawrth final four landing sites, respectively. MSL landing simulations indicate the probability of failure due to landing on a rock higher than the rover belly pan is 0.30%, 0.17%, 0.03% and 0.08% at Eberswalde, Gale, Holden, and Mawrth, respectively. Because these probabilities are less than the engineering requirement of <0.5%, all sites are safe with respect to rocks and rocks were not a factor in landing site selection.

Introduction

The size-frequency distribution of rocks on the surface of a planet is important for understanding the geologic processes that formed the surface (e.g., Garvin et al. 1981; Craddock et al. 2000; Ward et al. 2005; Yingst et al. 2007, Yingst et al. 2010; Grant et al. 2006), for determining the aerodynamic roughness important for eolian processes (Hebrard et al. 2012), for quantifying the hazards to landing spacecraft, and for evaluating the traversability for roving (Golombek and Rapp 1997; Golombek et al. 2003a; Golombek et al. 2008a). In the modern era of Mars exploration, increasingly sophisticated methods have been used to evaluate the rock abundance and distribution for certifying landing sites (e.g., Golombek et al. 1997; Golombek et al. 2003b; Golombek et al. 2012). During the Mars Pathfinder (MPF) project development and landing site selection (Golombek et al. 1997), Golombek and Rapp (1997) developed a model of the cumulative fractional area covered by rocks of a given size and larger based on measurements of rock diameters at the Viking Lander 1 and 2 (VL1, VL2) landing sites (Moore and Keller 1990, 1991), rock distributions at a wide variety of rocky locations on the Earth, and fracture and fragmentation theory (Rosin and Rammler, 1933; Gilvarry, 1961; Gilvarry

and Bergstrom, 1961), which predicts that ubiquitous flaws or joints will lead to exponentially fewer blocks with increasing size during weathering and transport (e.g., Wohletz et al. 1989; Brown and Wohletz 1995). The VL1 and VL2 rock distributions were fit by exponential equations of the form:

$$F_k(D) = k \, exp \, [-q(k) \, D], \qquad (1)$$

where $F_k(D)$ is the cumulative fractional area covered by rocks of diameter D or larger, k is the fraction of the total area covered by all rocks, and an exponential $q(k)$ that governs how abruptly the fraction of the total area covered by rocks decreases with increasing diameter (Golombek and Rapp 1997), which is approximated by

$$q(k) = 1.79 + 0.152/k. \qquad (2)$$

These distributions form a family of non-crossing curves (Figure 1) that flatten out at small rock diameter. Thermal differencing techniques using data from the Viking InfraRed Thermal Mapper (IRTM) instrument (Kieffer et al. 1977), were developed by Christensen (1986) to determine the area covered by rocks larger than around 10 cm (rock abundance) in 1° pixels. Because the area covered by rocks smaller than 10 cm diameter at the Viking sites is small, Golombek and Rapp (1997) used the IRTM rock abundance as an approximation of k, and determined that the area covered by rocks larger than 1 m diameter (corresponding to 0.5 m high

hemispherical rocks, which is roughly the stroke of the airbags) is about 1% for rocky areas on Mars like VL2 and the selected MPF landing site (~18% IRTM rock abundance; Christensen 1986). Rock distributions measured after the MPF landing were consistent with this expectation (Golombek et al. 1999, Golombek et al. 2003a).

During the Mars Exploration Rover (MER) landing site selection (Golombek et al. 2003b), Golombek et al. (2003a) reported on the complete MPF rock distributions, evaluated extreme boulder distributions in Mars Orbiter Camera (MOC) images, refined the fractional effective inertia of rock populations, and developed a formal method for determining the probability of encountering rocks larger than a given size based on the cumulative number of rocks of that size or larger per square meter and the area sampled by the lander. Models of the cumulative number of rocks of a given diameter or larger per square meter that are equivalent to those from equation 1 for any total rock abundance were developed by numerically integrating the cumulative fractional area curves (Figure 2). Rock abundance estimates from IRTM for the Meridiani and Gusev landing sites (Christensen 1986) were used along with the model distributions to estimate the cumulative number of rocks/m^2 and the probability of impacting rocks larger than 1 m diameter (Golombek et al. 2003a) for different numbers of airbag bounces. Predictions of the rock distributions based on the IRTM rock abundance and models for both sites were reasonably accurate (Golombek et al. 2005).
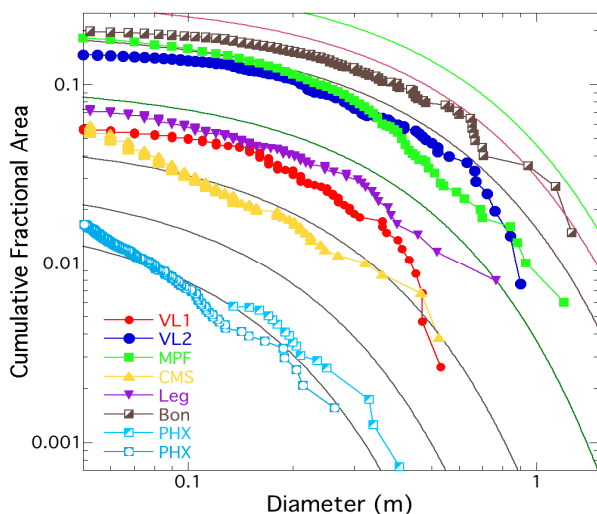

Figure 1. Cumulative fractional area covered by rocks versus rock diameter measured at the surfaces of the landing sites. Also shown are exponential model size-frequency distributions from equations 1 and 2 for 2%, 3%, 5%, 10%, 20%, 30% and 40% rock abundance (Golombek and Rapp 1997). Surface counts are: VL1 and VL2 from Moore and Keller (1990, 1991), MPF from Golombek et al. (2003b), Spirit Mission Success (CMS), Legacy (Leg) and Bonneville (Bon) from Golombek et al. (2005, 2006), and Phoenix from Heet et al. (2009) for intermediate areas and the largest rocks as described in the next section.

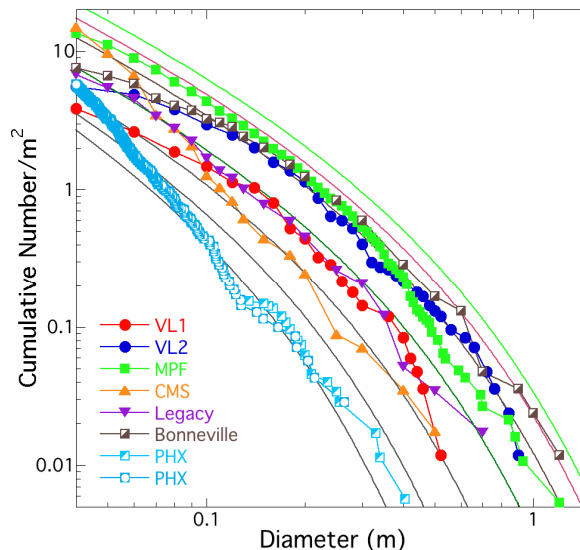**Figure 2.** Cumulative number of rocks greater than a given diameter per meter squared versus the rock diameter measured at the surface of the landing sites. Also shown are model size-frequency distributions derived by numerically integrating cumulative fractional area curves from equations 1 and 2 for 2%, 3%, 5%, 10%, 20%, 30% and 40% rock abundance (Golombek et al. 2003b). Data sources are the same as those described in Figure 1.

During the Phoenix landing site selection (Arvidson et al. 2008), the initial identification of landing site areas occurred before the Mars Reconnaissance Orbiter (MRO) was operational. No thermal differencing rock abundance estimates exist because water-ice clouds at high latitudes interfered with the method (Christensen 1986; Nowicki and Christensen 2007). Once MRO became operational, the High-Resolution Imaging Science Experiment (HiRISE; McEwen et al. 2007a) began imaging these areas at about 25 cm/pixel. To everyone's surprise and horror, most of the northern plains are covered by areas with dense boulder fields (McEwen et al. 2007b) that could not be avoided with the large landing ellipse of Phoenix and are far too rocky to safely land. Because of the low Sun angle of the images (about 36° above the horizon), large rocks cast long shadows. In addition, because the northern plains have relatively low relief with fairly uniform albedo, the shadows could be easily segmented from non-shadowed regions. The automated software fit ellipses to the shadows and circles to the rocks to accurately measure (within 1-2 pixels) rock diameter and height (by comparison to spacecraft of known size) of ~10 million rocks over >1500 km^2 of the northern plains (Golombek et al. 2008a). Rock distributions in these counts parallel exponential model curves above ~1.5 m diameter, and comparisons with surface measurements of rocky landing sites shows that HiRISE resolves the same population of rocks. As a result, the size-frequency distributions could be extrapolated along model curves to estimate the number of rocks at smaller diameters that could be hazardous to the Phoenix lander (Golombek et al. 2008a). Phoenix landed in a portion of the ellipse predicted to have low rock abundance. The estimate matched the dearth of large rocks found at the landing site (Heet et al. 2009).

Recently, Hebrard et al. (2012) used rock distributions from VL1, VL2 and MPF to fit a lognormal function and model for the rock size-frequency distributions on Mars to derive an aerodynamic roughness map for atmospheric and eolian studies. These lognormal model distributions for different rock abundances have shallower slopes at small rock diameters and steeper slopes at large rock diameters than the exponential model distributions and have been proposed as a better fit for these portions of the rock distributions at these three sites. However, the lognormal model Mars rock distributions proposed by Hebrard et al. (2012) shown in their Figure 14 do not parallel the measured rock distributions and become very steep (almost vertical on a log-log plot) as rock diameter increases so that almost no additional large rocks are predicted. As an example, the 20% lognormal rock abundance model curve that should roughly match the VL2 and MPF landing sites would predict almost no rocks larger than ~1 m diameter and the area covered by rocks >1.5 m diameter is more than 2 orders of magnitude less than expected for the equivalent exponential model. These differences are readily testable by considering measurements of rocks in HiRISE images with ~25 cm/pixel resolution. Golombek et al. (2008a) compared HiRISE and lander measurements of rocks distributions at the VL1, VL2 and MPF landing sites and found that in all cases the larger rocks resolved by HiRISE (>1.5 m diameter) are continuous

with lander derived rock distributions (<1 m diameter) and fall along similar exponential model distributions (and the same relationship is found in the next section for the Phoenix landing site). In the specific cases of VL2 and MPF that have lander measured rock abundance of ~20%, the lognormal model distribution predicts at least several orders of magnitude fewer large rocks and less area covered by rocks greater than 1.5 m in diameter than observed in HiRISE images. Similar discrepancies are also found at VL1 and Phoenix for lognormal models compared with HiRISE measurements. As a result, the lognormal model distributions proposed by Hebrard et al. (2012) would severely underestimate the actual risk to a landing spacecraft, which is most sensitive to the number (or area) covered by large rocks. These models are therefore not suitable for characterizing the size-frequency distribution of rocks important for landing spacecraft.

This paper describes the detection and characterization of rocks and rock size-frequency distributions of the four final Mars Science Laboratory (MSL) landing sites (Eberswalde crater, Gale crater, Holden crater and Mawrth Vallis) undertaken during the site selection and certification effort (Golombek et al. 2012). We begin by comparing the rock distributions estimated from orbit with those found at the Phoenix landing site. Next we describe improvements to the rock detection and mapping techniques that include deconvolution to sharpen the images, image partitioning to better accommodate image contrast, blur and noise in shadow segmentation, and the detection of shadows as small as 3 pixels (compared with 5 pixels for Phoenix). Because of the greater complexity of the terrain at the MSL landing sites, studies were conducted to identify and deal with the automated detection of shadows that are not rocks (e.g., hills, cliffs, scarps) that severely skew the cumulative size-frequency distributions. These studies showed that most of the non-rock detections are larger than 2.25 m and that the cumulative number of rocks/m^2 could be accurately fit to model distributions by the number of rocks 1.5-2.25 m diameter over 450 m square areas. Because of the high concentration of HiRISE images within the landing sites, overlap areas were tested for reproducibility, which is excellent. Finally, we describe the data products provided to the MSL project for landing simulations and rover traversability evaluations (e.g., Golombek et al. 2012) and discuss the results in terms of rock abundance, potential landing risk, comparison with rock distributions of past landing sites, and thermal differencing estimates of rock abundance.

Phoenix Landing Site Rock Distributions

Prior to landing Phoenix, the automated rock detection software was used to map out the density of rocks across the landing ellipse using the techniques and methods developed by Golombek et al. (2008a). A preliminary version of the rock density map of the landing ellipse was published in the Phoenix landing site selection paper (Arvidson et al. 2008), with a more complete version published by Spencer et al. (2009). Landing occurred in a portion of the ellipse with a

rock density of about one rock per hectare, which corresponds to a rock abundance of about 5% or less (Spencer et al. 2009; Golombek et al. 2008a). After landing, Heet et al. (2009) reported on several rock counts from the surface as well as in a HiRISE image of the landing site. Their hand count of rocks in the HiRISE image indicated a rock abundance of 3-4%, which is generally consistent with the surface counts in the sample area of the robotic arm for the largest rocks (~0.2 m diameter), but increases to higher rock abundances at smaller diameters (Heet et al. 2009). Because of the importance of using HiRISE rock counts to predict surface rock abundance for MSL, we took a closer look at the correlation of surface and orbital rock counts conducted for Phoenix, as a check on its predictive capability.

Heet et al. (2009) measured the diameter of all rocks in the 15 m^2 sample field area that could be reached by the robotic arm (area circled in red in Figure 3). In addition, they measured the long axis of rocks covering a greater (intermediate) area (70 m^2) around the lander (area circled in yellow in Figure 3) and categorized them according to their location within a trough or polygon (Heet et al. 2009). These two data sets were provided by Heet et al. (2009). The first data set includes the measurement of the long and short axes, which were averaged to get the rock diameters. The second data set includes the measurement of the longest axis of the rock. These measurements were multiplied by 0.75, because the average diameter of a rock is about 0.75 of its longest axis (Golombek and Rapp 1997; Golombek et al. 2003a). Finally, because some of the largest rocks were not included in either of these counts, we used the surface image mosaic projected into a Cartesian coordinate frame (Heet et al. 2009) to count the largest rocks in the 176 m^2 area around the lander (area circled in blue in Figure 3). The length and width were measured and averaged to get the diameter of the largest 27 rocks (0.13-0.4 m diameter). Rocks over a 250,000 m^2 area centered on the lander were measured by hand by Heet et al. (2009) in HiRISE image PSP_007853_2485 and we measured rocks using the automated rock counting software over 269,361 m^2 centered on the lander in PSP_008591_2485 (Figure 4).

Plots of the cumulative number of rocks per m^2 and cumulative fractional area versus rock diameter are shown in Figures 5 and 6, respectively. Counts of rocks by hand (Heet et al. 2009) and by the automated software in HiRISE images are similar in both plots and follow the model distribution for 3-4% rock abundance. Rock distributions for the three different surface counts are generally similar and follow the model distributions for 2-4% rock abundance for rock diameters greater than about 0.15 m. For diameters below 0.15 m, the surface rock size-frequency distributions are steeper than the models, similar to the Spirit landing site in the Gusev cratered plains than at other locations
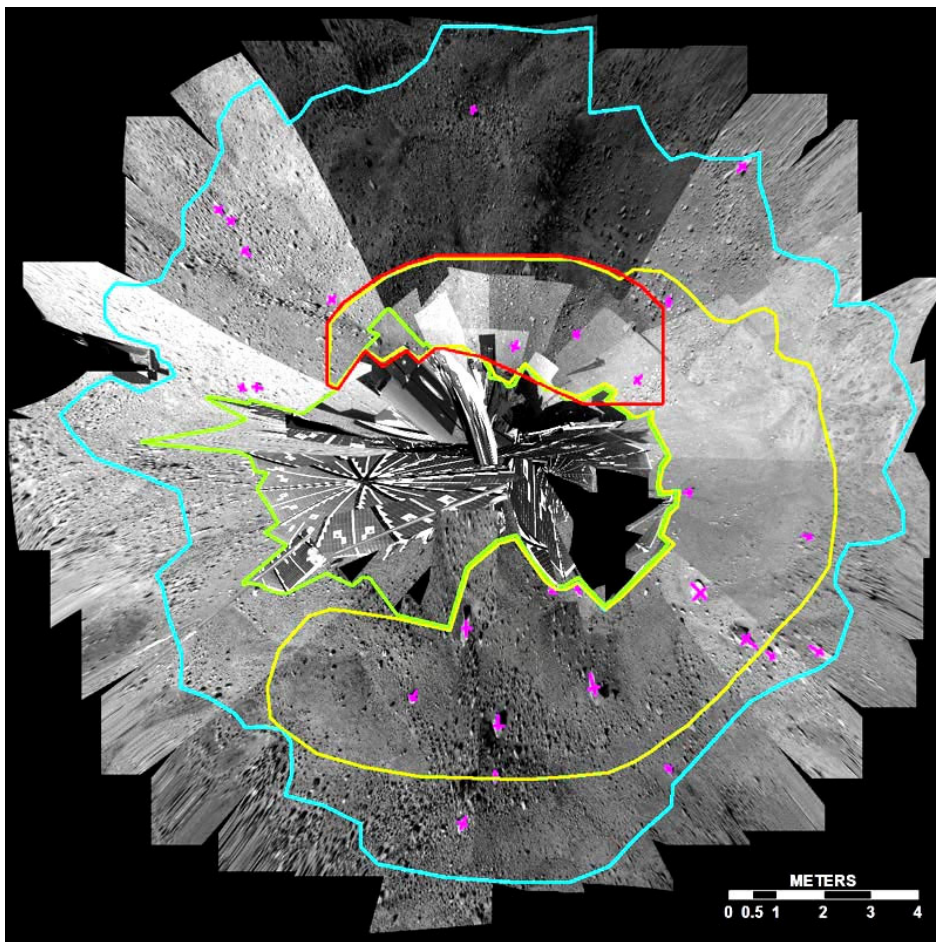

Figure 3. Phoenix surface images projected into a Cartesian coordinate frame from Heet et al. (2009) showing the three areas measured for rocks described in the text. The largest area outlined in blue, minus the central area made up of the lander shown in bright green is the 176 m^2 area in which the largest 27 rocks (0.13-0.4 m diameter) were measured (long and short axes shown in purple). The area outlined in yellow is the 70 m^2 area in which the longest axis of all rocks were measured. The area outlined in red is the 15 m^2 area of the sample field in which the long and short axes of every rock were measured.

where rock distributions have been measured on Mars (Golombek et al. 2006). This steeper trend probably relates to the different processes affecting rocks at these small diameters (cryoturbation at Phoenix, Heet et al. 2009, and wind sorting at Gusev, Ward et al. 2005). Of the three different areas around the lander where counts were made (Figure 3), the 15 m^2 sample (red) area has the highest density of rocks measured, the 70 m^2 intermediate (yellow) area the lowest, and the largest rocks in the 176 m^2 entire area (blue) is intermediate, with a density of rocks that parallels the model for 2-3% rock abundance. The rock size-frequency distributions measured at the surface for rocks >0.15 m diameter and in HiRISE images generally parallel exponential model distributions for rock abundances of 2-4%. Note that regardless of the use of a log-log plot, the different measured distributions match the exponential model to within 1-2%, which demonstrates the surface and orbital measurements are sampling the same population of rocks. These results are similar to those documented for the VL1, VL2 and MPF landing sites by Golombek et al. (2008a). They further validate using rocks measured in HiRISE images to extrapolate accurately to rock distributions with diameters smaller than 1.5 m diameter (down to about 0.1 m diameter) at the surface using the model.

The shape of the rock size-frequency distributions from the surface and in HiRISE images for the Phoenix landing site is poorly fit by the lognormal model distributions proposed by Hebrard et al. (2012). At small diameters the size-frequency distribution of rocks is much steeper than the flat (low slope) lognormal model curves and at large rock diameters the 2.5% and 5% rock abundance models applicable to the Phoenix site are so steep they would predict almost no rocks larger than 0.5-0.6 m diameter, whereas HiRISE measurements clearly show rocks larger than 1 m diameter. In contrast, as for the other landing sites, the exponential model distributions are parallel to the measured distributions for rocks larger than 0.2 m diameter and the

HiRISE measurements for rocks >1 m diameter fall along the same model distribution as the surface measurements.

In addition to reasonably accurately predicting the abundance and distribution of large, potentially hazardous rocks on landing, Golombek et al. (2008a) extrapolated the measured HiRISE distributions along the exponential model to predict the presence of small diameter rocks at the Phoenix landing site that could be moved by the robotic arm or that could depress the ground ice table. Specifically, rocks 2-10 cm in diameter were considered small enough to be moved by the robotic arm (Bonitz et al. 2008) and rocks >5
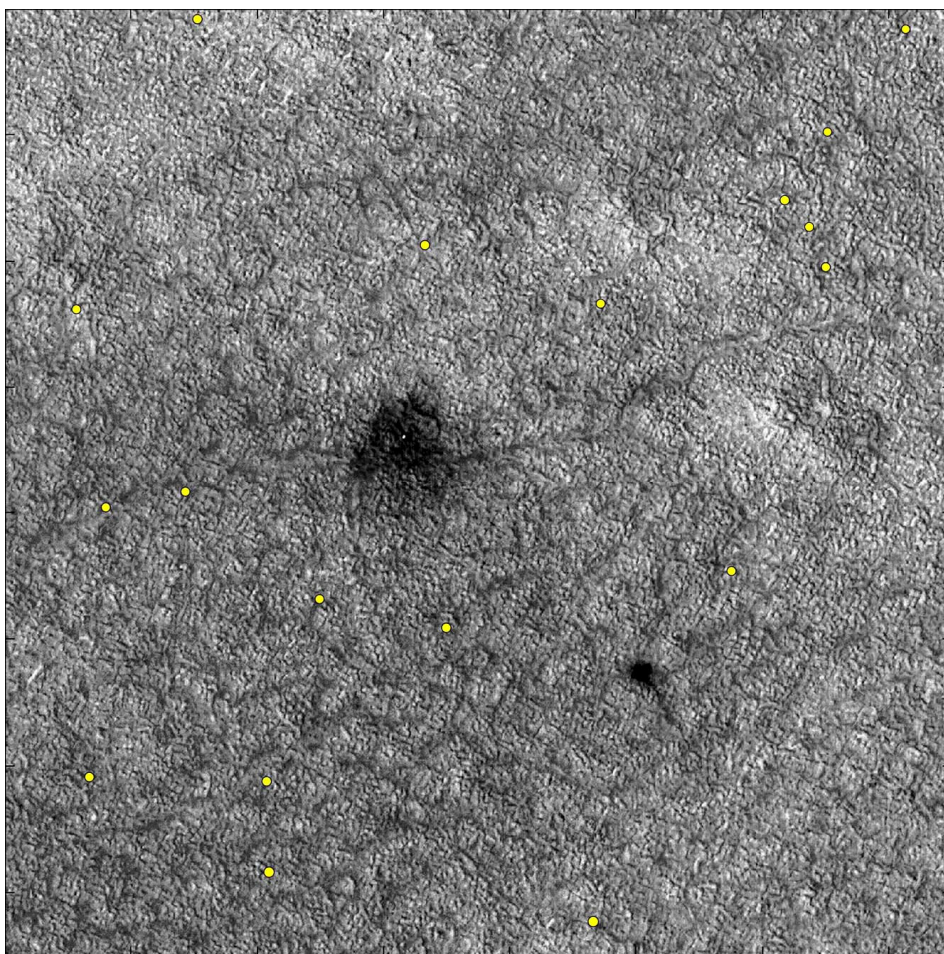

Figure 4. HiRISE image PSP_008591_2485 of the Phoenix landing site after landing. Image is 1500 pixels or 519 m on each side around the lander. The yellow spots are two times (for visibility) the segmented shadow pixels of rocks counted by the software. Lander itself (at the center of the dark area in the middle of the image) has been measured and removed. The dark area to the southeast was produced by the heat shield.

cm diameter were expected to depress the ground ice table (Sizemore et al. 2009). The number of rocks of this size range in the robotic arm workspace were estimated by extrapolation along the models from the measured rocks >1.5 m in diameter in HiRISE images. Results indicated multiple rocks of both size ranges were to be expected within the 3.8 m^2 area reachable by the robotic arm. These expectations were consistent with findings after landing with plentiful small rocks within the workspace, some of which

were moved by the robotic arm, and some of which were observed to depress the ground ice (Arvidson et al. 2009; Sizemore et al. 2010). Finally, Golombek et al. (2006, 2008a,b) discussed an observed relationship in which dustier landing sites have fewer small pebbles. The Phoenix landing site with its moderate albedo (a proxy for dustiness of the surface), compared to low-albedo portions of the Gusev cratered plains, would be expected to have a large population of pebbles comparable or greater than the model, which is what is observed.
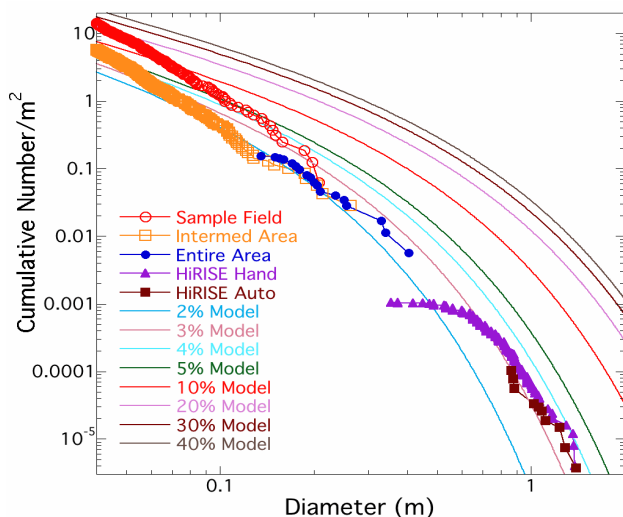
images to be selected that have very high signal to noise ratios (SNR, typically 200:1 for the 550-850 nm red non-map projected images processed for rocks), in order to improve their sharpness and contrast. Our objectives were to improve the accuracy of the rock detection derived from segmented shadows and to increase the number of smaller rocks detected. We conducted a number of experiments to look for a consistent deconvolution method (Gonzalez and Woods 1992) that could be applied systematically to sharpen the images covering the landing ellipses. Shadows cast by
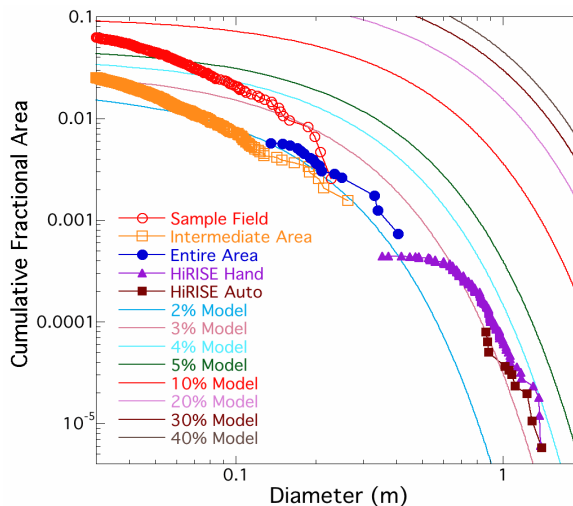

Figure 5. Cumulative number of rocks per m² greater than diameter, D, versus diameter for three areas measured at the Phoenix landing site, including an automated and hand count of rocks in HiRISE images and exponential model size-frequency curves for 2-40% rock abundance. The largest rocks at the landing site are parallel to model distributions of 2-3% rock abundance and appear continuous with rocks in HiRISE images that are parallel to model distributions of 3-4% rock abundance.

Figure 6. Cumulative fractional area versus diameter for three areas measured at the Phoenix landing site, including an automated and hand count of rocks in HiRISE images and exponential model size-frequency curves for 2-40% rock abundance. The largest rocks at the landing site are parallel to model distributions of 2-3% rock abundance and appear continuous with rocks in HiRISE images that are parallel to model distributions of 3-4% rock abundance.

Improved Rock Detection Techniques

The size-frequency distributions of rocks measured at the final four MSL landing sites are derived by applying an enhanced version of the automated rock measuring and counting procedure developed by Golombek et al. (2008a) for the Phoenix landing site selection in the northern plains. The enhancements are motivated primarily by the considerable increase in the complexity and diversity of the terrain in the proposed MSL landing sites compared with the relatively flat terrain and uniform albedo of the northern plains. The following improvements were incorporated: deconvolution methods to sharpen the images, detection of smaller rock shadows, improvements to shadow segmentation, and differentiation and elimination of shadows not produced by rocks.

Deconvolution Techniques

The extensive HiRISE image coverage of the proposed MSL landing ellipses (Golombek et al. 2012) allowed a subset of

rocks are salient features readily perceived by the naked eye. The observed images, however, have blurry shadow edges as can be expected, in most part, from inherent imperfections in the optics of the camera. Each light ray (point of light) passing through a lens is spread by the time it reaches the sensor. The spread is characterized by the point-spread function (PSF) of the optical system. The imaging process can be described by the following equation:

$$g(x,y) = f(x,y)*h(x,y) + n(x,y), \qquad (3)$$

where g is the observed image, f is the unknown, true image, h is the point spread function (PSF), n is noise and $*$ is the convolution operation. The observed image g therefore represents the true image f filtered, or convolved, with h, plus a noise component (due to electronics and quantum photons). With a high SNR in the observed image, we ignore the noise component and attempt to obtain a good approximation of f by deconvolving the PSF from g. In general terms, the convolution of the original image and the PSF is equivalent to the product of their Fourier transforms. By dividing this

product by the Fourier transform of the PSF, we are left with the Fourier transform of the original. The inverse transform then approximates the original image. Sharpened edges reduce the ambiguity in the location of the shadow edges making them easier to identify. The two major benefits are an increase in the accuracy of the measured width of the shadows of larger rocks, and the increased confidence in the detection of the smallest shadows (3 pixels).

To test these potential benefits in rock detection, we chose a dataset consisting of HiRISE sub-images around landers and rovers on Mars. These spacecraft provide a ground truth of known size, and the surrounding terrain includes rocks that are visible in both HiRISE images and surface images (e.g., Golombek et al. 2008a). We used at least two HiRISE sub-images of each of the MPF, VL1 and VL2, and the two MER rovers (Spirit and Opportunity). The deconvolution techniques that were tested include two iterative methods, blind deconvolution (BD) and Lucy-Richardson deconvolution (LRD), and two non-iterative methods, Wiener filter deconvolution (WFD) and regularized filter deconvolution (RFD) (Biggs and Andrews 1997; Hanisch et al. 1997). Except for blind deconvolution, these methods require knowledge of the PSF of the optical system and some knowledge of the image noise model to be effective.

The BD and LRD techniques iteratively update the recovered image by repeatedly re-blurring the recovered image and comparing it with the observed image. The difference is used to update the restored image and the process is repeated for a given number of iterations or until a constraint on the difference is met. The implementation used employs a Maximum Likelihood Estimator (MLE) during each iteration (Holmes et al. 1995). The iteration is designed based on a probability model and the mathematical solution is the restored image f that has the highest probability of being correct. Strictly, BD does not require knowledge of the PSF but estimates one from the iterated updates. In our implementation an estimated PSF was used to seed the process and thus reduce the number of iterations needed. This makes BD and LRD essentially equivalent.

WFD and RFD, on the other hand, are not iterative but use the inverse filter and regularization filter methods respectively (Gonzalez and Woods 1997, Jain 1989). In WFD the method uses an approximate direct linear inversion of equation 3 without noise and requires a noise model to attempt to remove it from the restored image in the process (Gonzalez and Woods 1997, Jain 1989). RFD uses a regularized filter and implements a least squared solution where constraints on the output image can be made (e.g., a smoothness requirement). A noise model is also required to avoid noise amplification.

In the process of choosing a specific deconvolution technique that could be applied systematically to all the HiRISE images in the dataset we need to have, or theoretically define, the PSF of the system. We conducted experiments using the Lorenzian approximation of the PSF described by Kirk et al. (2008) derived from star images in the Stellar M calibration sequence. The 21x21 narrow (0.77

pixels) Lorenzian filter, with 50% of the signal for a given pixel coming from features three or more pixels away, produced very sharp results. These results, however, were not consistent for all the images in our data set. Noise pixels in small dark, non-shadow regions could result in many false alarms at the scale of the smallest rocks.

The results of our deconvolution experiments lead to the following conclusions: a) WFD and RFD require accurate noise models to prevent artifacts and noise amplification. The noise models are image dependent and thus the methods are less practical for systematic processing of large datasets. RFD attempts to preserve image smoothness, thus minimizing noise magnification but performed inconsistently for all the images in the test set. The iterative methods, BD and LRD, perform well consistently for all images in the dataset. The LRD method requires a PSF whether measured or theoretically estimated. The BD method does not require a PSF and will estimate one obtaining an improved approximation with each iteration. In our experiments we designed a small number of narrower Gaussian PSFs with space constants of 0.75, 1.0, 1.25 and 1.5 pixels. These narrower filters assume a more restricted influence of the neighboring pixels than the Lorenzian filter. In fact, the experiments with the narrower Gaussian PSFs gave the most consistent results with minimal artifacts and noise amplification. We also used the Gaussian PSFs to seed the BD method PSF approximation. In particular, using BD seeded with a 7x7 Gaussian PSF with space constant $\sigma=1.0$ pixels yielded the most consistent results for all the images with no discernable artifacts or false shadow detections. Results with the LRD were similarly consistent, as well. The experiments with blind BD and LRD required a few iterations to obtain good image restoration. Our experiments agreed with previous work (Biggs and Andrews 1997) on iterative deconvolution approaches that indicate a leveling-off of the mean square error after four iterations. To sharpen the HiRISE images of the MSL landing sites therefore, we used BD, a 7x7 Gaussian PSF, and four iterations.

Shadow Segmentation

Processing HiRISE images for the Phoenix landing site selection indicated that shadow segmentation was able to reliably and robustly detect and analyze shadow regions with ≥ 5 pixels (~ 0.4 m^2) in their umbras (Golombek et al. 2008a). With the images sharpened by deconvolution, we were able to improve that limit to just 3 pixels (~ 0.24 m^2). This development results in a significant increase in the number of smaller rocks detected. Our deconvolution experiments indicate that the resolution roll off (the rock diameter at which all rocks are not detected) could decrease, in many images, from about 1.5 m to 1.2 m in rock diameter. Figures 7 and 8 illustrate blind deconvolution examples for two Mars Pathfinder landing site sub-images. Among the rocks is the Pathfinder lander, which casts a shadow and is the third largest "rock" in the scene. The "rock" size estimates are 1.87 m wide and 0.89 m tall. In the restored image, the lander is 1.42 m wide and 0.9 m tall. Actual dimensions projected according to the MPF lander orientation and sun
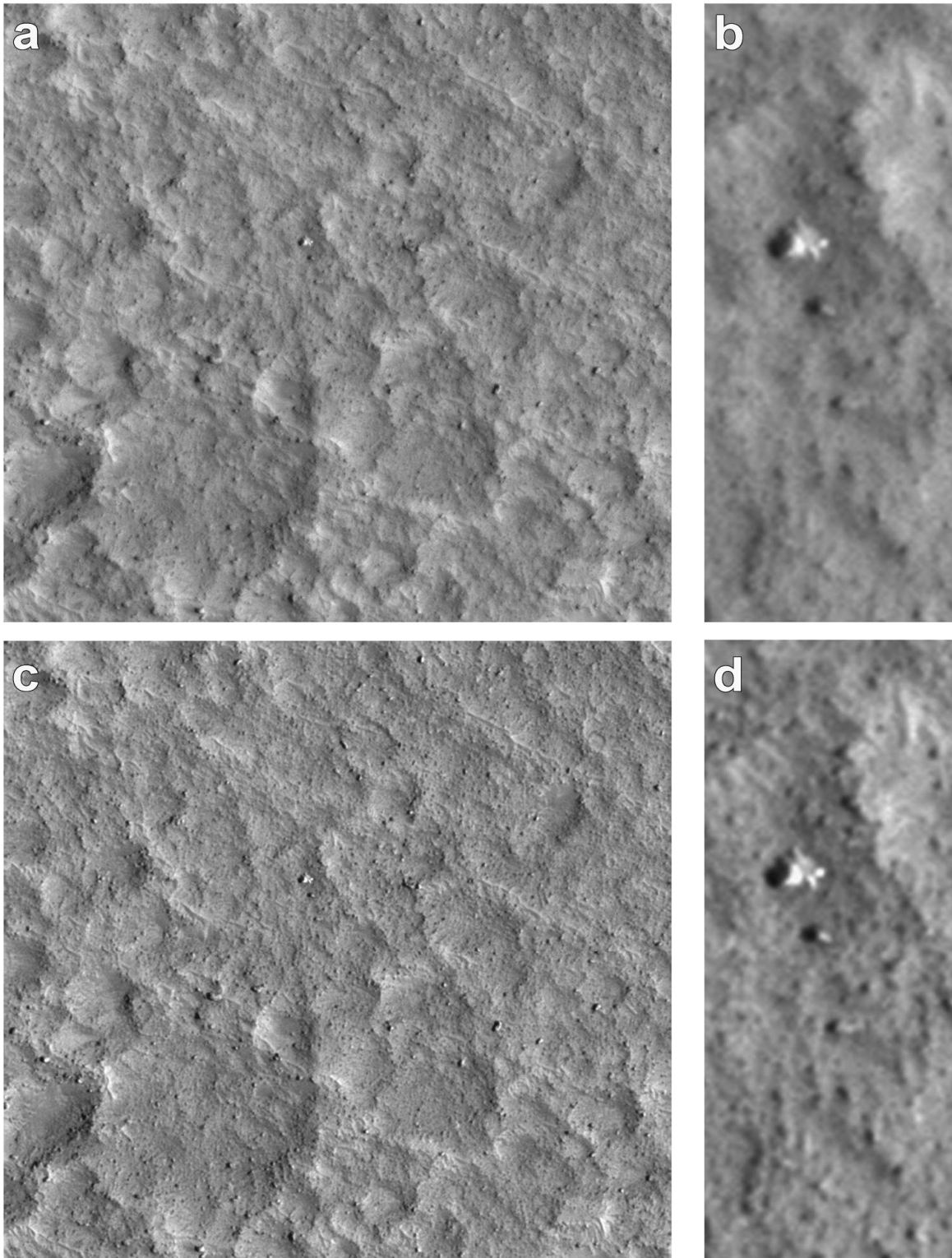
Figure 7. Sub-image (185 m x 185 m) of HiRISE PSP_001890_1995. Top row: original image (28.5 cm/pixel) and detail of the MPF lander. Bottom row: sub-image sharpened by deconvolution using a 7x7 Gaussian point spread function (σ=1.0).

azimuth are 1.4 m wide and 0.9 m tall showing that deconvolution sharpening improves our estimates of rock diameter and height.

The rock detector incorporates two adaptations that tune its analysis to image contrast and remaining blur and noise (Golombek et al. 2008a). The first adaptation is related to the image pre-processing step implemented to enhance the shadow regions while attenuating the background details. Applying non-linear gamma-correction to the images has the effect of increasing the distinction between the shadow regions and the rest of the image by increasing the saliency of the shadows to a point where the image intensity histogram becomes bi-modal. A very-fast 1-D histogram analysis determines automatically the intensity threshold below which a pixel is in shadow. While a single threshold applied to the entire image gives very good shadow segmentation

Figure 8. Detail of lower-left portion of the images in Fig. 7 and size-frequency of rocks in a similar sub-image (not shown) from PSP_002391_1995. Top row: rock shadows (≥5 pixels) from the original image. Bottom row: rock shadows (≥3 pixels) from the sharpened image. Dark lines are 5%-40% rock abundance exponential models (Golombek & Rapp 1997). Automated counting yields an increase from 43 and 65 rocks from two original sub-images of the site, PSP_001890_1995 and PSP_002391_1995 respectively, to 230 and 360 rocks counted in the sharpened sub-images. Bottom row: sub-image sharpened by deconvolution using a 7x7 Gaussian point spread function (σ=1.0)

results, our implementation of shadow segmentation is further optimized by processing the image in 500x500 pixel tiles. The segmentation threshold is derived locally and optimally for each tile. A connected-components algorithm then groups the shadow pixels into regions that are described by best-fit ellipses that are quickly assessed for size and orientation. Shadow regions that pass this size filtering step are considered candidates for rock detection and modeling; they are analyzed in detail to derive measures of shadow width and length from which a rock model is derived (Golombek et al. 2008a). The width of the shadow is approximated by the diameter of a circle fit to the shadow width at the terminator of the rock. The shadow is fit by an

ellipse, the length of which determines the rock height using the Sun elevation angle. The rock height estimate assumes that the local surf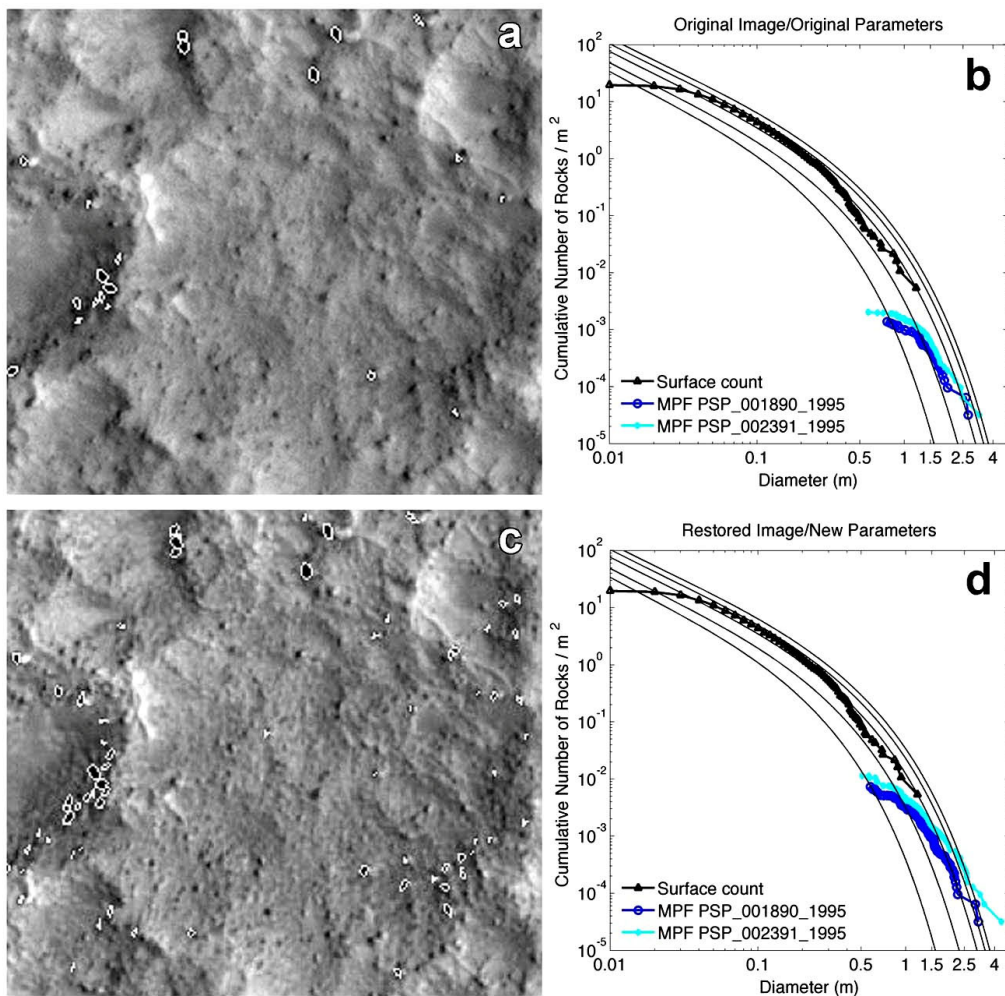ace is flat and level. This assumption could be adjusted with knowledge of the local topography from a digital elevation model (DEM) of the terrain. This step involves an analysis of the local slope errors and remains to be incorporated.

The second adaptation in the rock detection process is related to the illumination intensity gradient across the rock-shadow discontinuity. Most rock shapes will exhibit a sharp illumination boundary. Softer intensity transitions typically correspond to isolated features that are not rocks (e.g., small hills, mounds and fragmented eroded escarpments). The gradient parameter in our system allows filtering out, in part, such non-rock features with great success when applied to images of the northern plains where boulders and other

terrain features could be readily distinguished. In some portions of the MSL landing sites, however, the ambiguity remained and additional analysis was needed to remove shadows that are not cast by rocks.

A third rock detection and mapping improvement was motivated by the variability of the terrain topography and surface albedo that can be present in a single image. This suggested processing each image in a number of sections, to allow finer tuning the parameters that drive the adaptations described above, and then combining the results. While the optimal sectioning of the images should ideally conform to geomorphic or albedo units, for practical purposes we partitioned the images along the HiRISE image length in eight equal-size sections. While we did not formally quantify the impact of sectioning the images, the empirical result analyzed qualitatively showed a modest improvement for the sites that have less variation in geomorphology (Eberswalde and Holden) and a more significant improvement at the sites with increased local or broader albedo variation (Mawrth and Gale). A secondary benefit of 8-section image partitioning is that deconvolution of large HiRISE images (20,048 pixels x N, with N varying from 60,000 to 100,000 pixels at ~0.3 m resolution) is challenging for standard desktop computers. All other processes handle the images in a tiled fashion as described earlier, and run on standard desktop computers.

Elimination of Non-Rocks and Model Fit

The automated process has a limited ability to differentiate non-rocks that cast shadows, such as portions of escarpments, small hills and mounds, from actual rocks. Potential non-rock hazards that cast shadows are illustrated in Figure 9. Because most of these non-rocks tend to be larger than rocks, they have a large effect on the cumulative size-frequency curves, making correlation with model distributions difficult. This correlation becomes important to allow extrapolation of rock abundance to rock sizes that are not fully resolvable by the rock detector at HiRISE resolution. Full

resolvability is at about 1.5 m diameter rocks that on average are 0.75 m high, a height that still exceeds the 0.6 m high belly pan of the MSL rover. To address this gap it was necessary to differentiate rocks from non-rocks. The rock population can then be correlated with the size-frequency distribution models for Mars to predict local rock abundance and hence, the landing and traversability risk due to rocks.

To differentiate rocks from non-rocks, user-assisted tools were developed that allow operators to classify non-rocks and exclude them from the maps. This was tested in a pilot study that evaluated 4 zones (each a square with 1.05 km sides) selected for diversity in each landing site. The four pilot study zones in the Gale crater site are shown in Figure 10. The rock detector processes the images in 500 x 500 pixel tiles (about 7 tiles 150 m x 150 m each) and keeps explicit information of the detections associated with each tile. Within the zones, an operator excluded non-rocks allowing comparison of the size-frequency distributions before and after editing. Results showed that most non-rocks are greater than 2.25 m in diameter and that, after editing, the
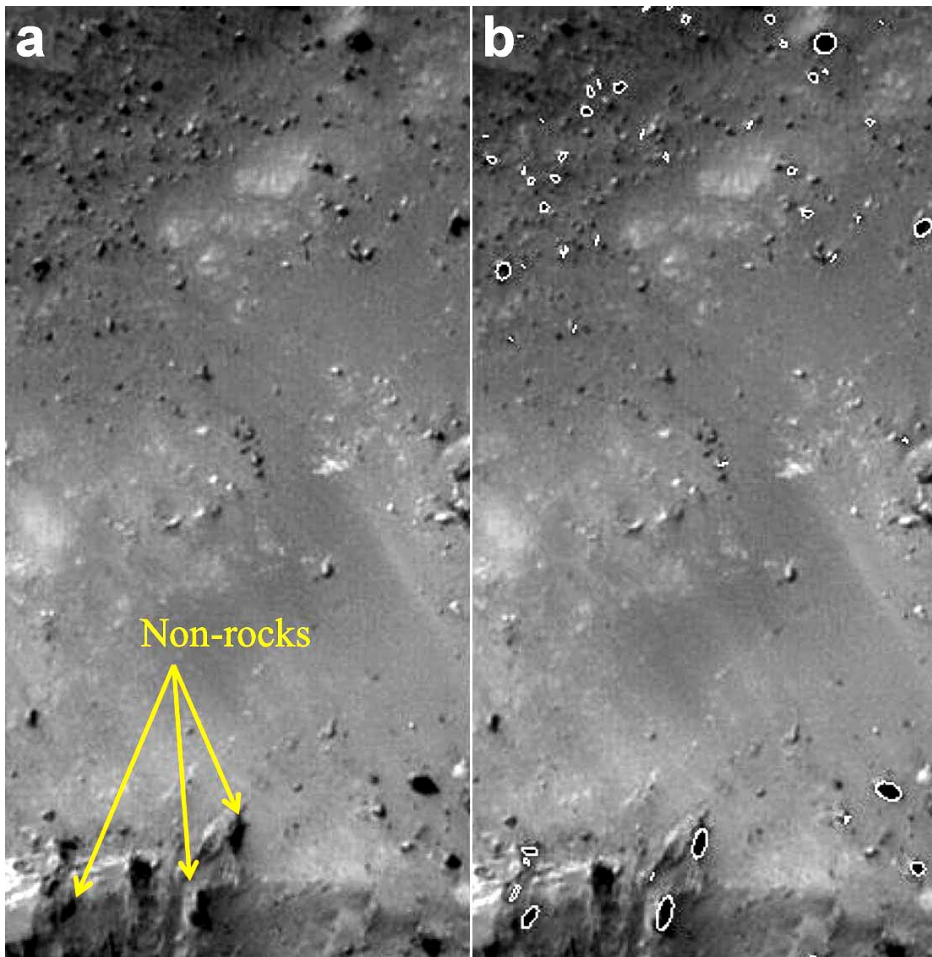

Figure 9. Some features that cast shadows are counted as rocks. Non-rocks are excluded (see text) from the detected rock population to allow correlation with the Mars rock size-frequency distribution model, and to facilitate extrapolation to smaller, undetected rocks that remain hazardous to the rover.

size-frequency distributions followed the model distributions. Figure 11 shows the classification tool with one 150 x 150 m tile (with 50-pixel overlap) and segmented shadows. Figure 12 illustrates the size-frequency distribution before and after the exclusion of non-rocks. As can be seen, the size-frequency distribution of rocks closely follows the model distributions after editing. Non-rocks remain in the dataset provided to the project because they remain hazardous to landing and roving.

Editing by an operator was considered to eliminate the non-rocks and to select the best fit exponential model rock abundance. However, there are more than 17,000 tiles that are each 150 m square that cover the landing sites. Editing each tile takes an experienced operator 10-15 min. As a result, it would take a single operator more than 1 yr to edit all the tiles if they worked 8 hrs/day, 5 days a week! As a result, we looked for an automated way to edit out the non-

diameter is unique for each individual rock abundance model distribution, the measured number of rocks 1.5-2.25 m in diameter matched only one model rock abundance.

To test this method, we used the pilot study zones, which had been edited by an operator so we could judge the automated fits. Trials with different numbers of tiles showed that 450 m square areas (composed of 9 square tiles, each 150 m across) had enough rocks to adequately define the size-frequency distribution between 2.25 m and 1.5 m diameters. Results for three examples are shown in Figure 12 for a portion of the Gale pilot zone 8 shown in Figure 10. In Figure 12, all detections by the software are shown in red, the operator edited size-frequency distribution of rocks after removal of the non-rocks are shown in blue, and the automated best fit model is shown in dark yellow. The operator-edited distribution (blue) matches the automated best fit distribution (d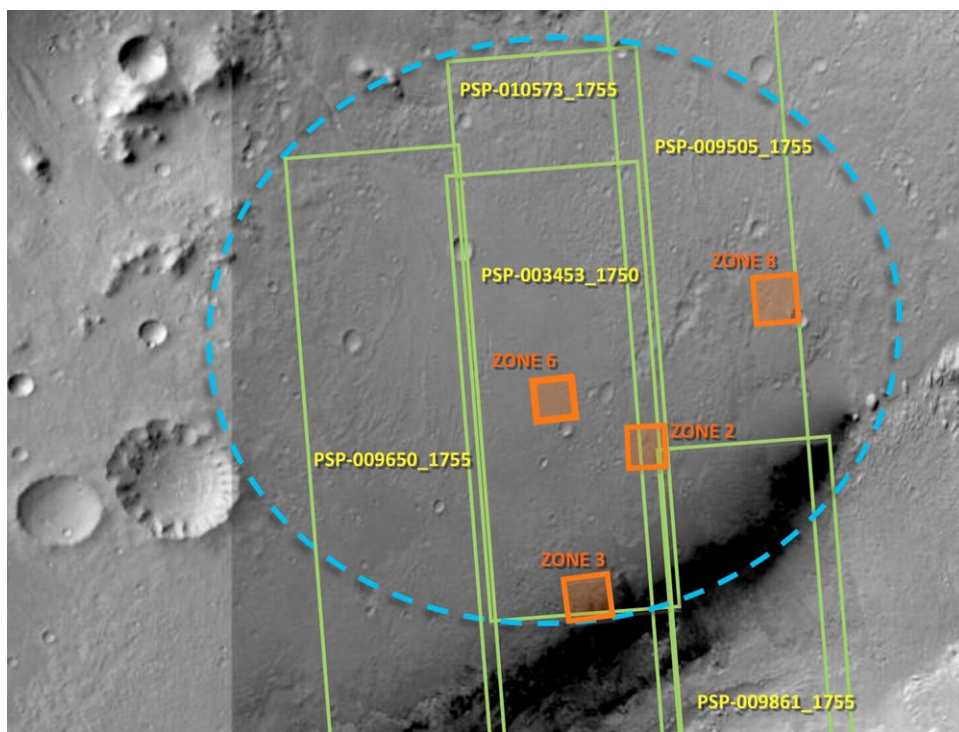ark yellow), which indicates that the automated procedure removes the non-rocks and accurately fits the appropriate model size-frequency distribution. Figure 13 shows the HiRISE image containing Gale pilot zone 8 from which the example in Figure 12 is taken and also shows the HiRISE image, the rock density in 150 m tiles, the detail of Gale pilot zone 8 and the derived cumulative fractional area derived from the model fit.

Figure 10. Example landing ellipse in Gale Crater (blue) and the HiRISE coverage for rock detection (green). Four representative zones, ~1 km² each (orange), were interactively edited to exclude non-rocks for rock abundance estimation.

After selecting both the range of rock diameters and the size of the region over which to perform a model fit, the process of estimating the local rock distribution from the image processing results was automated. This was accomplished by the generation of a lookup table that related the total number of rocks 1.5-2.25

rocks and to fit the measured rocks to the best-fit model distribution. Because our pilot study indicated that most non-rocks are >2.25 m in diameter and the resolution roll off for rocks is about 1.5 m, we decided to select the cumulative number of rocks within this size interval. The cumulative number of rocks per m² greater than 2.25 m diameter was subtracted from the cumulative number of rocks greater than 1.5 m diameter that were measured. This yielded the total number of rocks 1.5-2.25 m in diameter in the area. Next the same subtraction was performed for the model distributions of cumulative number of rocks per m² for different rock abundances, k. Because the number of rocks 1.5-2.25 m

m in diameter in a given 450 m x 450 m pixel area to the model of cumulative fractional area covered by rocks. Table 1 shows the number of 1.5-2.25 m diameter rocks per 450 m square pixel expected for every 1% increment in model rock abundance from 1% to 30%. This process yielded non-integer values for the number of rocks for each model rock abundance. As can be seen, one rock in a 450 m square pixel corresponds to about 4.1% of the surface covered by rocks. The lookup table was generated from these model distribution numbers according to the integer number of rocks observed per 450 m pixel. For each pixel, the number of observed rocks was linked with the lowest model rock

abundance that yielded an estimated number of rocks greater than or equal to the observation (Table 1). This process, due to rounding upwards, yields an overestimation of the local rock abundance. The overestimation of the local rock abundance is desired to add conservatism to the engineering safety assessment process. Additional conservatism was added by assuming at least one rock was present in each pixel, even where none were measured. This resulted in a minimum rock abundance of 5% for any pixel, even if no rocks were actually present. These are the values provided to the project for landing simulations.

To better characterize the actual rock abundance, we also performed the same model fit without inflation and to higher
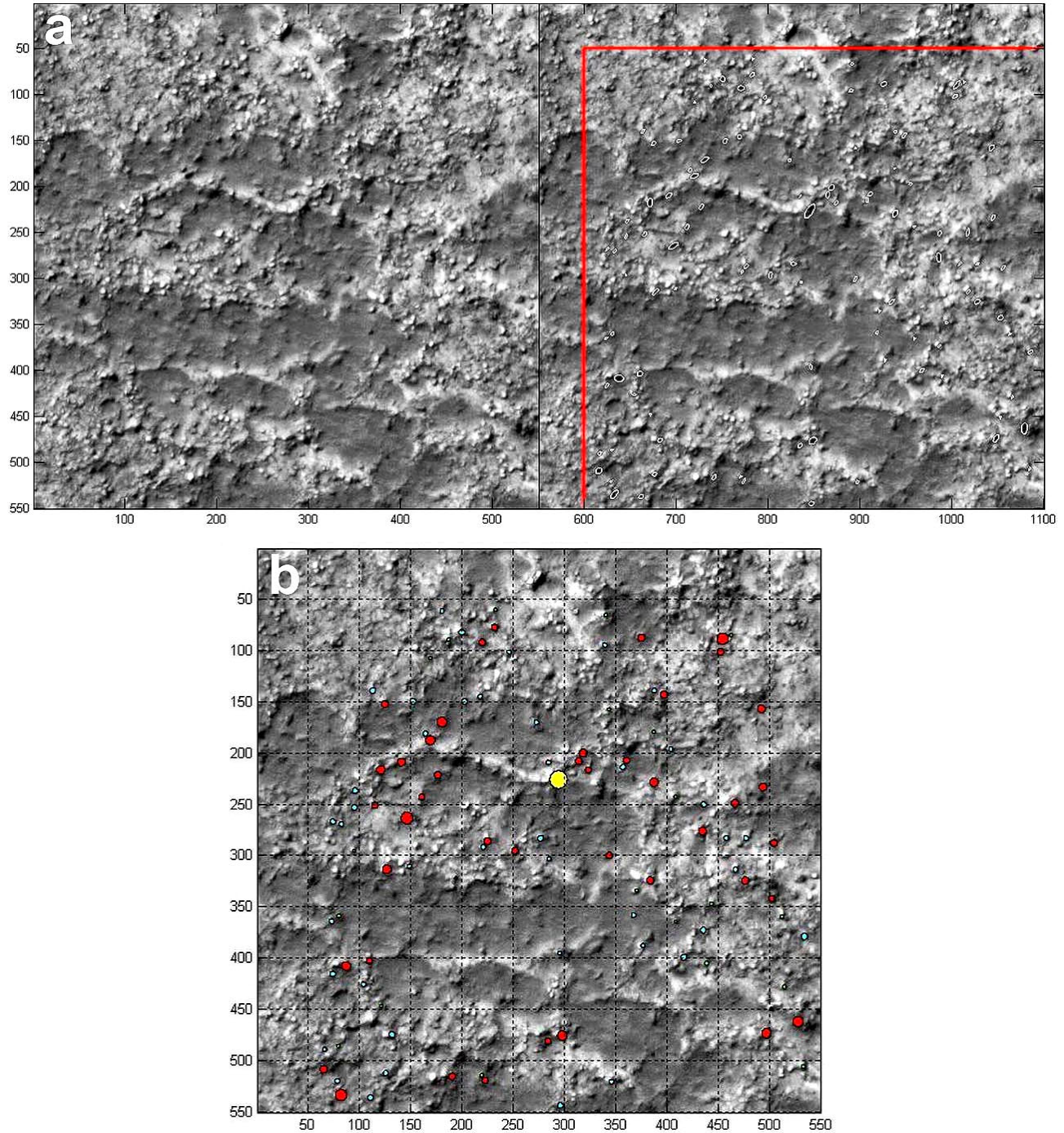

Figure 11. The classification tool allows operator to visualize rock detector output and interactively mark non-rocks. a) Image tiles (~150 m on the side plus ~15 m overlap) and segmented rock shadows overlaid are recorded during the automated counting process. b) An interactive pane shows detected rocks (red and blue are 1.5-3.5 m and 1-1.5 m diameter, respectively). User-selected rocks, turned yellow by a mouse click, are identified and recorded as non-rocks.
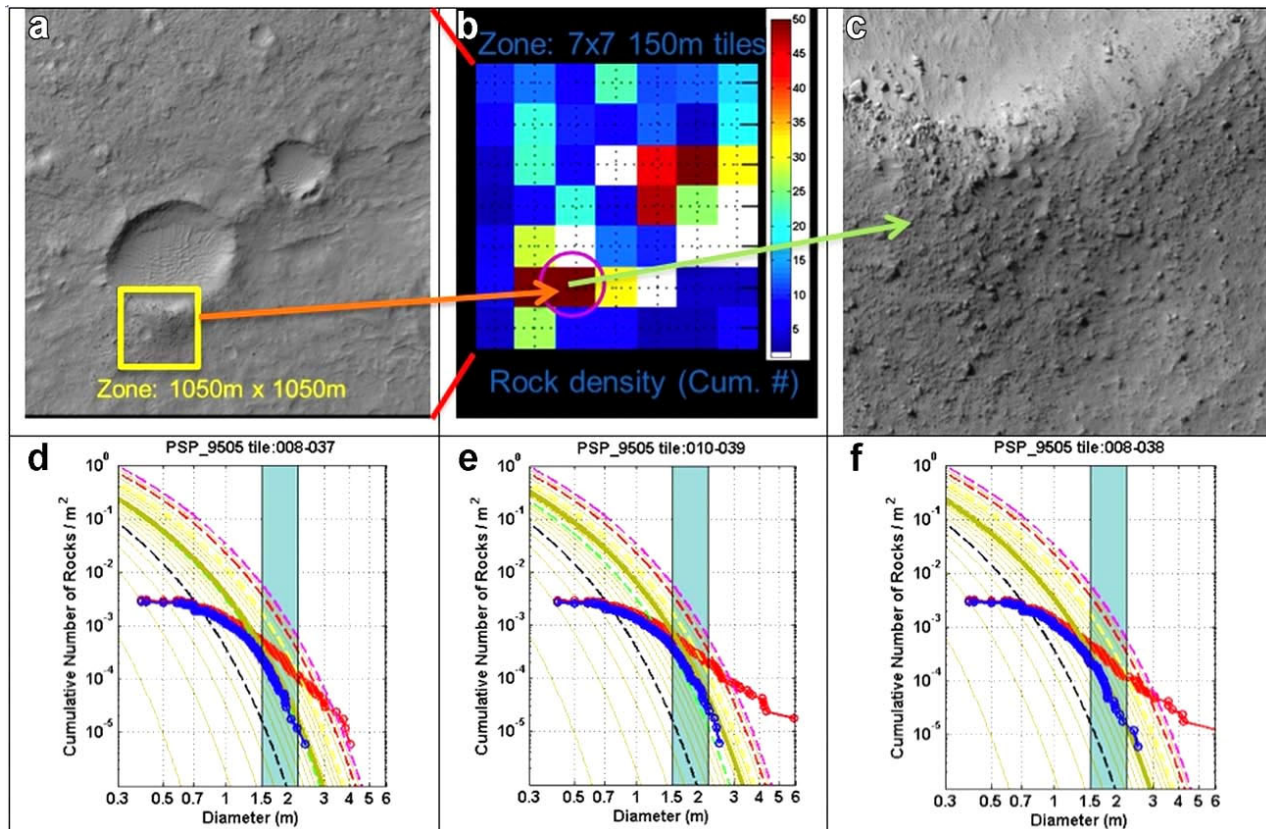
Figure 12. Work flow showing estimation of rock abundance, creation of a rock density map, editing out non-rocks, and fitting the model rock abundance. Top row shows: a) HiRISE sub-image of zone 8 in Gale Crater, b) the corresponding rock density in the 49 tiles covering the zone, and c) a sharpened sub-window of one of the tiles. The bottom row shows: three (d, e, f) cumulative number of rocks/m^2 versus diameter plots using 450m-side square area (9 tiles) around each 150m pixel in the map. The plots show all rocks detected by the software (red curve), the rock density remaining after excluding non-rocks by hand (blue curve), and the best-fit model distribution (thick, dark yellow curve) derived from the number of rocks 1.5-2.25 m diameter (shaded green interval). Dashed lines are exponential model distributions (Golombek and Rapp 1997) for 5% (black), 10% (green), 20% (yellow), 30% (red) and 40% (pink) rock abundance.

accuracy. In this process, a revised lookup table that related the integer total number of rocks (1-669) 1.5-2.25 m diameter in a given 450 m x 450 m pixel are fit to the best model cumulative fractional area covered by rocks at one tenth increments (Table 1) up to 30%. In this process, 450 m bins without any rocks are assigned a 0% rock abundance (as opposed to 5%). Because the area covered by a 450 m pixel is only 202,500 m^2, a pixel with just one rock corresponds to a model cumulative fractional area of 4.1%. To get lower rock abundances would require areas for pixels of 1.5 km, 9 km and 12 km, for which one rock would result in model cumulative fractional areas of 3.0%, 2.1% and 2.0%, respectively. Because such large pixels would reduce the resolution of the measurement and smooth out differences in rock abundance, we accept this dichotomy between 0% and 4.1% rock abundance for 0 and 1 rock, respectively, in 450 m pixels.

Results

Rock Density

The average number of rocks in 150 m tiles ranges from 0.3 at Holden crater to 13.3 at Eberswalde crater, with Gale crater and Mawrth having 7.7 and 3.7, respectively (Table 2). The maximum number of rocks in 150 m tiles varies from 442 at Eberswalde to 48 at Holden. The average number of rocks in 450 m bins ranges from 2.5 at Holden to 83.9 at Eberswalde, with Gale and Mawrth having 57.2 and 27.7, respectively (Table 2). The maximum number of rocks in 450 m bins varies from 3119 at Eberswalde to 205 at Holden. These numbers actually refer to the total number of detections and include a small number (<1%) of non-rocks (scarps, hills and mounds). The number of rocks 1.5-2.25 m diameter in 450 m bins are far fewer than the total number of rocks detected (<15%). Because the number of rocks larger than 2.25 m diameter is small, most of the difference is due to rock detections smaller than 1.5 m diameter, which are excluded due to the resolution roll off. The total number of rocks in 450 m bins correlates well with the number of rocks 1.5-2.25 m diameter at most of the sites. An example for Eberswalde is shown in Figure 14, which shows an excellent fit between the two, with rocks 1.5-2.25 m in diameter comprising 15% of the total number of rocks. Table 2 shows the ratio of rocks 1.5-2.25 m in diameter with the total

number of rocks for all 4 sites as well as the correlation coefficient between the two. We find similar relations and fits at Gale and Mawrth (ratio and correlations coefficient are 0.13 and 0.12, and 0.94 and 0.90, respectively), but a lower ratio (0.03) and poorer fit (0.67) at Holden, where the total number of rocks is small and a larger fraction of the total are non-rocks. Rock heights are varied, but are generally less than half their diameter, averaging from 0.29 to 0.41 for Eberswalde, Gale and Holden (Table 2).

The density of rocks at the final four MSL landing sites is shown in Figure 15. The figures show the total number of rock detections found within 150 m square tiles. The greatest number of detections for all of the landing sites is associated with hills and mesas in the western portion of Eberswalde crater, where the number of rocks routinely exceeds 100. Most of the rest of the ellipse contains a patchwork of 1 to 20 rocks per 150 m tile. Gale crater has dense rock detections that typically exceed 20 rocks per 150 m tile in the southeast and southwest portions of the ellipse, with the rest of the ellipse having few rocks. Mawrth detections are relatively low (<8) throughout most of the ellipse, but spike to higher

numbers (>20) around craters and mesas scattered throughout the ellipse, and are concentrated to the north and northwest. Holden has very few rocks. Outside of detections of non-rocks along the eastern edge of two central images, most of the ellipse has no rocks with a scattering of <8 detections to the west (Figure 15).

Rock Abundance

The rock abundance at the landing sites was determined by fitting the cumulative number of rocks 1.5-2.25 m in diameter in 450 m bins to the model cumulative fractional area distribution using the two methods described earlier. To evaluate how well the fits encompass the actual measurements, we plotted the number of rocks in each 450 m bin with the best fit model rock abundance (Figure 16). Because the model fit is based on only the rocks 1.5-2.25 m diameter, we used the relationship at each site derived between the total number of rocks and the number of rocks 1.5-2.25 m in diameter to plot the model rock abundance derived from the fit. That best fit line rises steeply from the origin (0 rocks and 0% rock abundance) to 4.1% rock
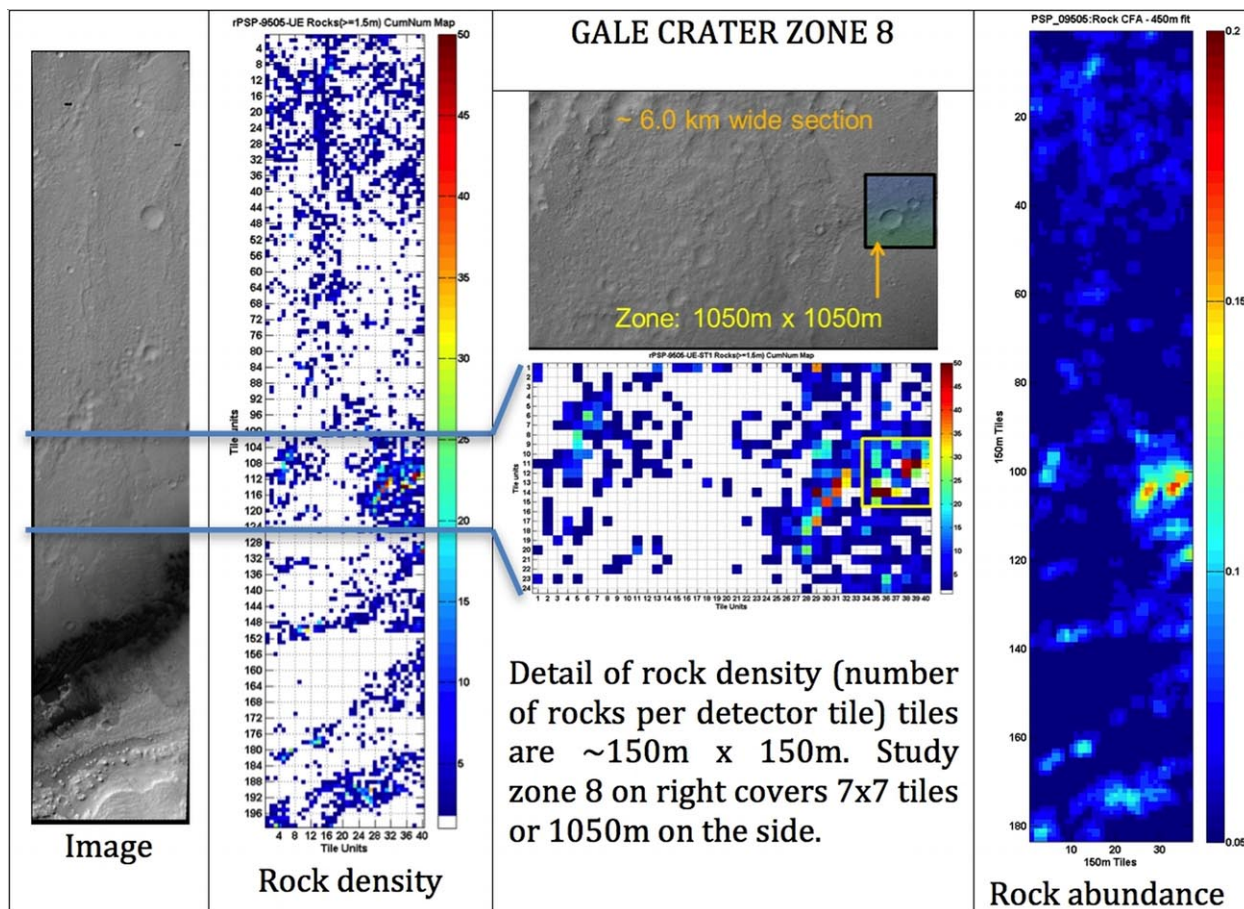

Figure 13. Rock density and cumulative fractional area maps for the HiRISE image containing the Gale pilot study zone 8. From left: HiRISE image PSP_009505_1755 covering the east-of-center portion of the landing ellipse in Fig. 10. The corresponding 150 m detector tiles showing the number of rocks. Detail of the image and rock counts around the 7x7 tile pilot study zone 8. Map of the estimated cumulative fractional area covered by rocks in 450m bins spaced every 150 m. See text for discussion, Figure 10 for location of this pilot study zone and Fig. 12 for examples of the model rock abundance fits.

Table 1. Number of rocks 1.5-2.25 m diameter and corresponding cumulative fractional area (CFA) of rocks in 450 m bins used for landing simulations and characterization.

Number of Rocks	CFA[1] (%)	CFA[2] (%)
0	5	0
1-3	5	4.1-5.0
4-8	6	5.3-6.0
9-15	7	6.2-7.0
16-26	8	7.1-8.0
27-40	9	8.1-9.0
41-56	10	9.1-10.0
57-75	11	10.1-11.0
76-96	12	11.1-12.0
97-119	13	12.1-13.0
120-144	14	13.1-14.0
145-170	15	14.1-15.0
289-320	20	19.1-20.0
455-489	25	24.1-25.0
633-669	30	29.1-30.0

[1]CFA rounded up for landing simulations.
[2]CFA to closest tenth of a percent used for analysis.

images for shadow enhancement, shadow segmentation, fitting ellipses to shadows and cylinders to rocks to derive rock diameter, elimination of non-rocks and fitting to a model rock distribution for rocks 1.5-2.25 m in diameter. Because the images were processed independently with no consideration of the other image, the comparison can be considered as a blind test of the reproducibility. HiRISE images PSP_010573_1755 and ESP_018920_1755 in the southwest, center part of the Gale ellipse have 245 overlapping 450 m cells (4.8 km by 7.8 km) and images ESP_011331_1560 and ESP_019190_1560 in the east, central part of the Eberswalde ellipse have 316 overlapping 450 m cells (3.7 by 15.8 km). Results for the cumulative fractional area derived for landing simulations are almost identical (mean and standard deviation) for the overlap areas: 6.5±2.2% versus 6.2±2.0% for Gale and 6.7±1.5% versus 6.6±2.2% for Eberswalde. Comparison of the difference in the best fit model rock abundance for overlapping bins shows that over 80% of the estimates are within 1% and over 95% are within 2% of the derived rock abundance. Because the difference in the probability of landing on a potentially hazardous rock is less than 0.05% for a difference of 1% rock abundance for these sites (see later discussion), the 5-20% of bins with different rock abundance will have no appreciable impact on the simulation results and the reproducibility of the estimated rock abundance is excellent.

For the method that quantized and rounded up to the next higher cumulative fractional area for the landing simulations,

abundance for ~8 rocks (1 rock 1.5-2.25 m in a 450 m bin divided by the ~0.15 ratio of total rocks to those 1.5-2.25 m in diameter). The fit then progressively shallows similar to a partial exponential derived by integrating the cumulative fractional area exponential relation in equation 1. The model fit similar to the overall shape of the distribution of total number of rocks versus rock abundance data (Figure 16), indicating that the method to derive the model rock abundance is describing the overall distribution of the measurements.

The overlapping image areas in which the rock abundance was measured and fit to a model cumulative fractional area provide an estimate of the repeatability of the method. Of the 4 landing sites, Gale and Eberswalde have overlaps of 250 or more 450 m bins. The overlapping HiRISE images were independently processed using the method described in earlier sections, including: blind deconvolution, segmentation of the

Table 2. Rock statistics in the MSL landing sites.

Landing Site	Eberswalde	Gale	Holden	Mawrth
Rocks in 150 m bins, Mean±SD	13.3 ± 23.8	7.7 ± 16.6	0.3 ± 1.8	3.7 ± 8.2
Range	0-442	0-398	0-48	0-201
Number of bins	16,474	11,031	14,684	16,616
Rocks in 450 m bins, Mean±SD	83.9 ± 164.3	57.2 ± 96.9	2.5 ± 10.0	27.7 ± 45.8
Range	0-3119	0-1048	0-205	0-793
Number of bins	1,918	1,904	1,691	2,283
Total number of rocks	160,938	108,888	4,215	63,354
Rocks 1.5-2.25 m in 450 m bins, Mean±SD	11.4 ± 26.5	7.0 ± 13.8	0.1 ± 0.5	3.6 ± 5.8
Range	0-546	0-171	0-6	0-65
Total number of rocks	21,913	13,287	192	8,168
Ratio All/1.5-2.25 m, r[1]	0.15, 0.98	0.13, 0.94	0.03, 0.67	0.12, 0.90
CFA[2] (%) in 450 m bins Mean±SD	5.4 ± 2.6	3.9 ± 3.0	0.3 ± 1.1	3.3 ± 2.7
Range	0-27	0-15	0-6	0-11
n	1,918	1,904	1,691	2,283
CFA[2] (%) in 450 m bins used in landing simulations, Mean±SD	6.6 ± 1.9	5.8 ± 1.4	5.0 ± 0.3	5.6 ± 0.9
Height-diameter ratio[3]	0.29	0.36	0.54	0.41

[1]Ratio of 1.5-2.25 m diameter rocks divided by all rocks, r is correlation coefficient.
[2]CFA is cumulative fractional area covered by rocks as described in the text.
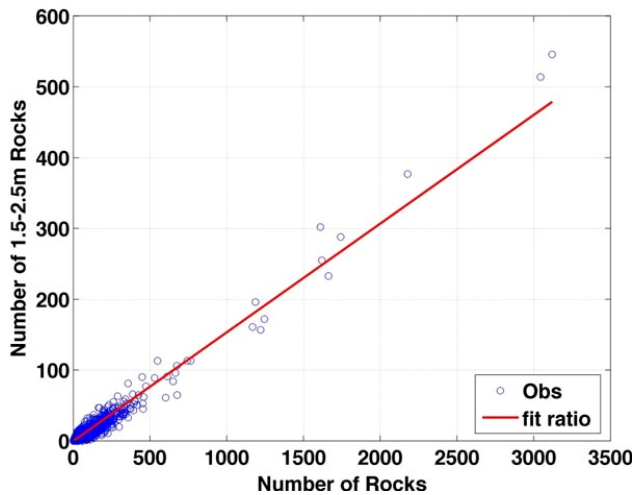[3]Average height, diameter ratio of all 1.5-2.25 m diameter rocks.

Figure 14. Plot of the total number of rocks detected versus the number of rocks 1.5-2.25 m diameter in 450 m bins for the Eberswalde landing site. The linear fit has a slope of 0.15 and a correlation coefficient of 0.98.

average rock abundance at Eberswalde, Gale, Holden and

Mawrth are 6.6±1.9%, 5.8±1.4%, 5.0±0.3% and 5.6±0.9%, respectively. As discussed these numbers are inflated and overestimate the actual average rock abundance. The second method, which fits to the closest tenth of the cumulative fractional area and includes bins with 0% rock abundance, yields lower average rock abundances at Eberswalde, Gale, Holden and Mawrth that are 5.4±2.6%, 3.9±3.0%, 0.3±1.1% and 3.3±2.7%, respectively. Maximum rock abundance at Eberswalde, Gale, Holden and Mawrth are 27%, 15%, 6% and 11%, respectively.

The maps of the best-fit cumulative fractional area covered by rocks at the landing sites are shown in Figures 17 and 18. The Figure 17 map fits the rocks 1.5-2.25 m diameter in 450 m by 450 m grids spaced every 150 m to the size-frequency rock model with a 5% minimum rock abundance binned in 5% rock abundance intervals. Figure 18 fits the 1.5-2.25 m diameter rocks in 450 m bins to the size-frequency rock model with no minimum. Both maps show similar distributions of rocks, although Figure 18 is at a coarser resolution than Figure 17 and shows areas with no rocks. Of the landing sites, Eberswalde has the highest rock abundance and the highest concentrations of rock abundance and
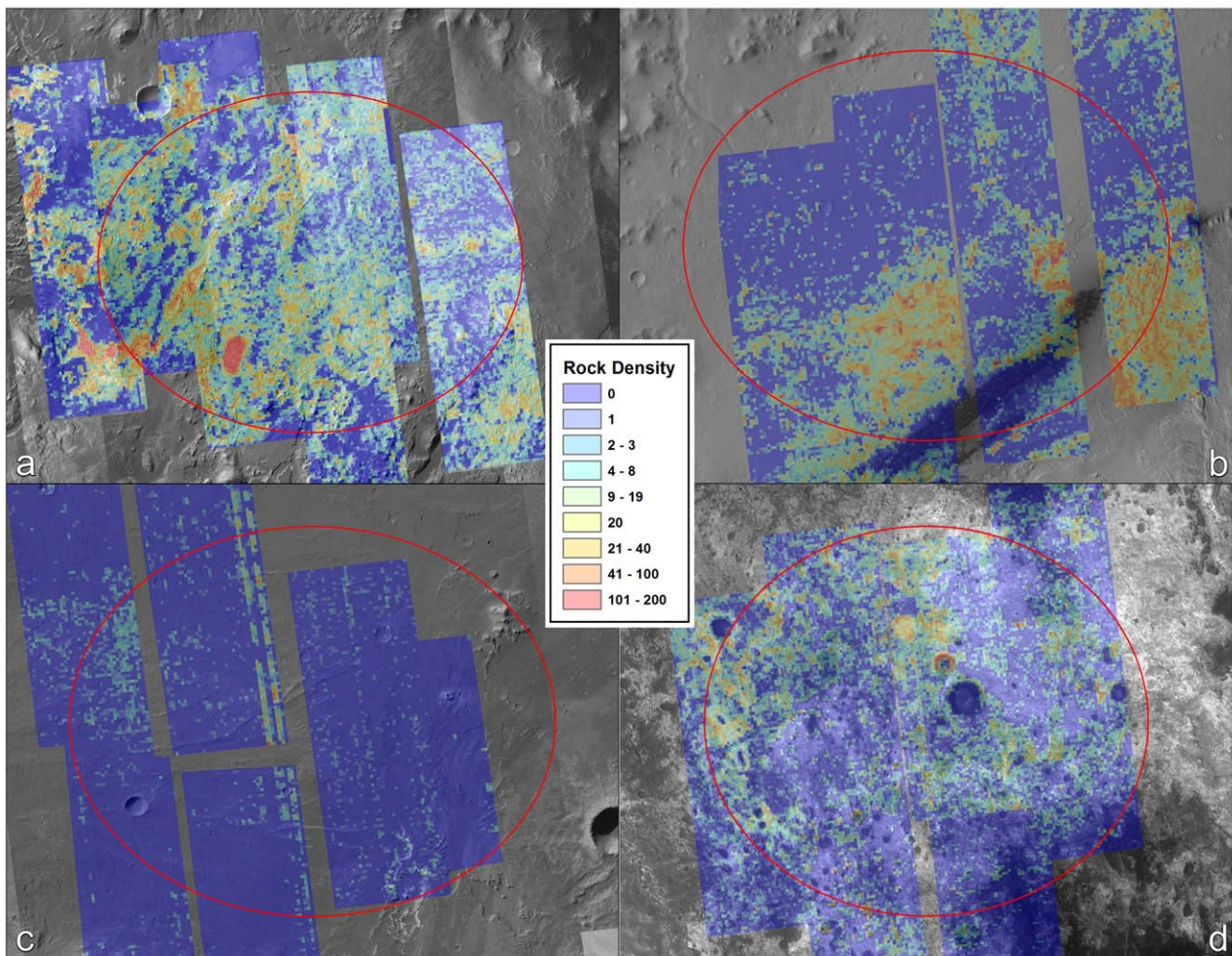

Figure 15. Density of rocks at the final four MSL landings sites: a) Eberswalde, b) Gale, c) Holden, and d) Mawrth. The density is the total number of rocks measured in 150 m square tiles prior to model fitting and so some non-rocks (e.g., Holden) have not been corrected. See text for discussion.

Holden has the lowest. Eberswalde has broad tracks of the ellipse covered with 5-10% cumulative fraction area covered by rocks and it has multiple concentrations of rock abundance >10% in hills and mounds concentrated in the western part of the ellipse, including one with 27% of the area covered by rocks. Holden has most of the ellipse covered by no rocks, although some areas scattered around the ellipse and in the "go to" troughs to the southeast have higher rock abundances. Gale is also somewhat rocky with broad tracks with 5-10% area covered by rocks (particularly in the southern part of the ellipse), and with small areas that rise to 10-15% rocks. Mawrth has most of the ellipse covered by a patchwork of <5% and 5-10% area covered by rocks (Figures 17 and 18) with a few small concentrations that rise to 11%.

Discussion

The total area covered by measured rocks 1.5-2.25 m diameter in HiRISE images of the landing sites is small and measures 0.011%, 0.006%, 0.00006% and 0.004% at Eberswalde, Gale, Holden, and Mawrth, respectively. We subtracted the model size frequency distribution for the cumulative fractional area covered by rocks >2.25 m diameter from those >1.5 m diameter for one tenth increments in total rock abundance to derive the best fit total average rock abundance. The total rock abundances derived from this method are 6.1%, 5.6%, 2.8% and 5.0% for Eberswalde, Gale, Holden, and Mawrth, respectively. These numbers compare favorably within one standard deviation of the averages of the best fits for 1.5-2.25 m diameter rocks derived from the 450 m binned data for all sites except Holden, which could be due to the small sample of rocks at this site.

Average rock abundances of 4-5% for Eberswalde and Gale compare favorably to the rock abundances at the Gusev cratered plains (the landing site has a rock abundance of around 5%) ([Golombek et al. 2005](#); [Golombek et al. 2006](#)). The average rock abundance of around 3% for Mawrth Vallis is similar to the Phoenix landing site. The average rock abundances were also extrapolated along the model size frequency distributions to derive the area covered by rocks >0.1 m diameter, which corresponds to the rock abundance
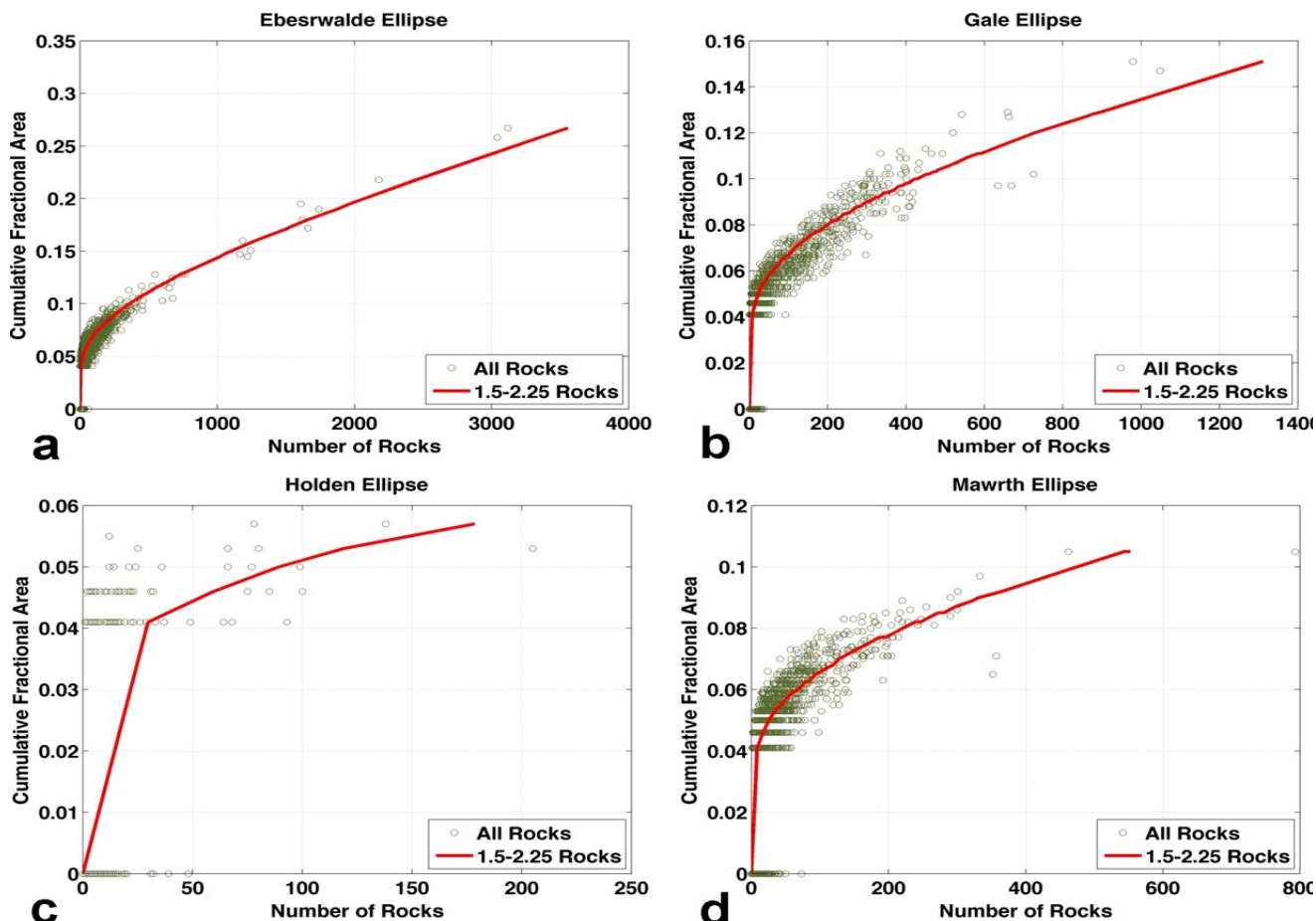

Figure 16. Plots of the total number of rocks in 450 m bins with the best fit model rock abundance for Eberswalde (A), Gale (B), Holden (C) and Mawrth (D). Because the model fit is based on only the rocks 1.5-2.25 m diameter, the relationship at each site derived between the total number of rocks and the number of rocks 1.5-2.25 m diameter was used to plot the model rock abundance derived from the fit.

estimated from thermal differencing (Christensen 1986; Nowicki and Christensen 2007). Results suggest that the landing sites have equivalent thermal rock abundances of 4.1%, 3.6%, 1.4% and 3.1% for Eberswalde, Gale, Holden, and Mawrth, respectively.

Thermal differencing rock abundance estimates from IRTM (1 pixel per degree) and TES (8 pixels per degree) for the landing sites are higher than those measured in HiRISE images (compiled in Golombek et al. 2012). IRTM rock abundance estimates average 10%, 10%, 11%, and 14% (Christensen 1986) for Eberswalde, Gale, Holden, and Mawrth, respectively. TES rock abundance estimates (Nowicki and Christensen 2007) are less continuous and even higher, averaging 45%, 19%, 35%, and 27% for Eberswalde, Gale, Holden, and Mawrth, respectively (although TES data for Gale and Holden are from the edge of the ellipses). This discrepancy can be explained by the preponderance of layered outcrop at the sites, which would appear as rock thermally, but not as individual rock hazards, for which the size-frequency model distributions were developed.

Bulk rock abundances of <7% indicate the probability of encountering one rock higher than the 0.55 m (corresponding to a 1.1 m diameter rock) under the rover during touchdown is <0.5% (using the method in Golombek et al. 2003a; Golombek et al. 2008a; Golombek et al. 2012) and thus meet the engineering criterion for safe landing. The engineering requirement is that the probability of damaging the rover via landing on high rocks must be a small fraction of the total allowable failure probability for entry, descent and landing (Golombek et al. 2012). This allocation implies the probability that a rock taller than the 0.55 m high clearance (assumed to be 1.1 m diameter for hemispherical rocks) occurs in a random sampled area of 4 m^2 (the area of the belly pan including the area out to the wheels) should be less than 0.5% for the proposed sites. Because measured average rock abundances for the landing sites are <6%, all of the sites comfortably meet this engineering requirement and are safe for landing.
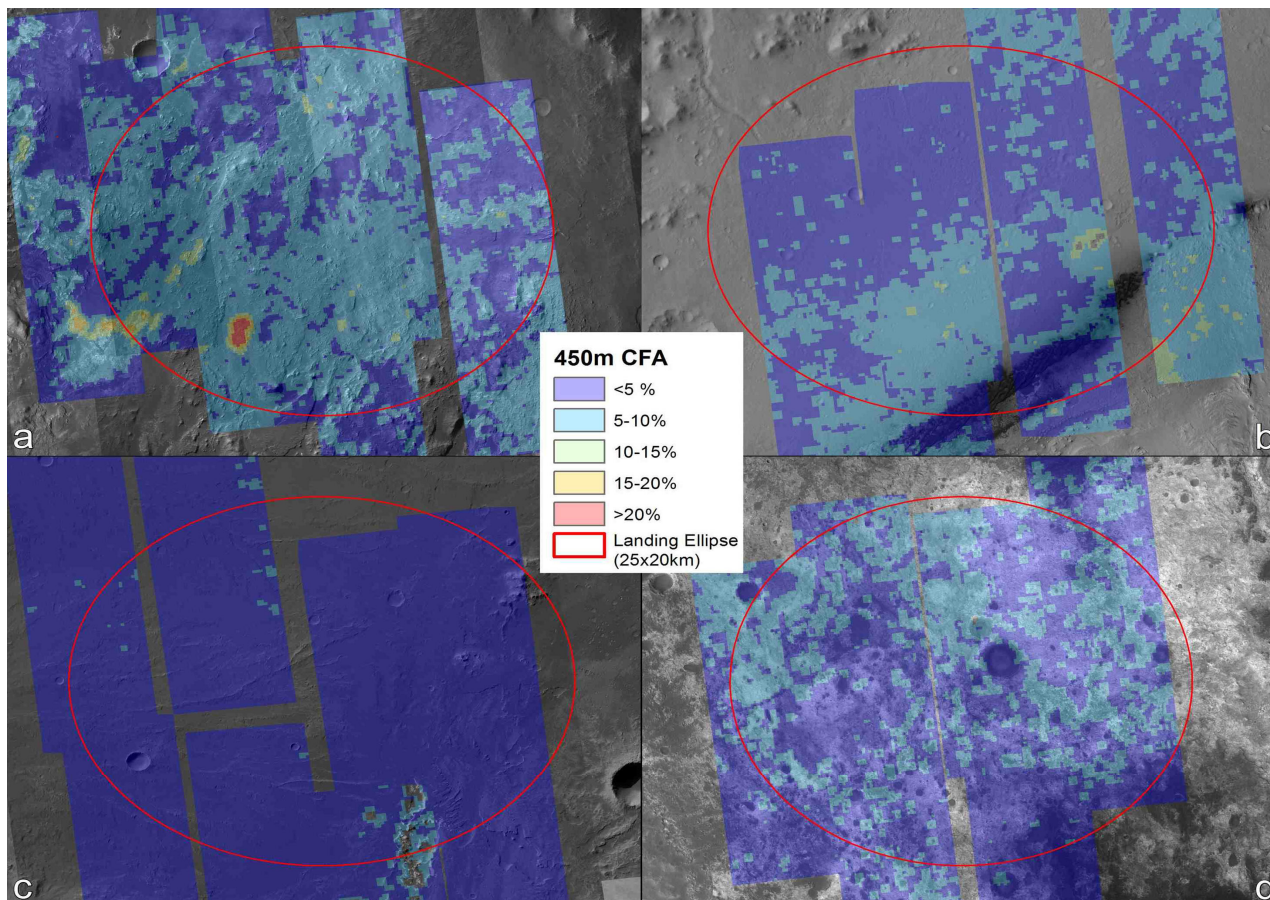

Figure 17. Maps of rock abundance at the final four MSL landing sites: a) Eberswalde, b) Gale, c) Holden, and d) Mawrth. Rock abundance is derived from rocks measured in HiRISE images in 450 m square areas fit to the model cumulative size-frequency distribution for rocks 1.5-2.25 m diameter with a 5% minimum, sampled every 150 m as described in the text. These maps were provided to the MSL project for landing simulations.

Subsequent testing and analysis has indicated that the area of greatest concern is just that of the belly pan, which is 2.682 m^2 (Golombek et al. 2012), which can safely fit rocks 0.6 m high during touchdown. The landing simulations assume hemispherical rocks, that rocks larger than 1.2 m in diameter will pose a hazard to the belly-pan at touchdown, and that rocks larger than 2.25 m diameter will pose a threat to the mobility system. Because the area of the belly pan is less than the underside of the rover out to the wheels, the probability of encountering a potentially hazardous rock is lower. As examples, for 5-10% rock abundances, the probability of impacting rocks >1.1 m diameter and >1.2 m diameter in 4 m^2 and 2.682 m^2 areas is 0.08% - 0.75% versus 0.027% - 0.31%, respectively, a factor of 2 difference. Note that all of these probabilities are considered worst case because they assume hemispheric rocks even though the measurements show the rock height to diameter ratio is less (0.3-0.4 at the rocky sites). Table 3 relates the total number of rocks in 150 m tiles illustrated in Figure 15, the total number of rocks 1.5-2.25 m diameter in 450 m bins, the cumulative number of rocks per square meter larger than 1.1

and 1.2 m in diameter, the equivalent rock abundance, and the probability of the rover landing on 1 rock larger than 1.1 and 1.2 m diameter for the different assumed areas.

The landing simulations convolve the probability of landing at a particular point in the ellipse with the probability of failure due to landing on rocks >1.2 m diameter under the belly pan (as well as detections >2.25 m diameter) at that location to yield a combined probability of failure due to rocks at each site (e.g., Golombek et al. 2012). The resulting probability of failure is 0.30%, 0.17%, 0.03% and 0.08% at Eberswalde, Gale, Holden, and Mawrth landing sites, respectively. Interestingly, the risk of landing on rocks <2.25 m diameter is 0.039%, 0.035%, 0.027% and 0.03% compared to 0.26%, 0.14%, 0.0002%, and 0.051% from detections >2.25 m for Eberswalde, Gale, Holden, and Mawrth landing sites, respectively. In all cases, the convolved probabilities for impacting rocks meet the engineering constraint for the landing sites and thus were not a factor in landing site selection.
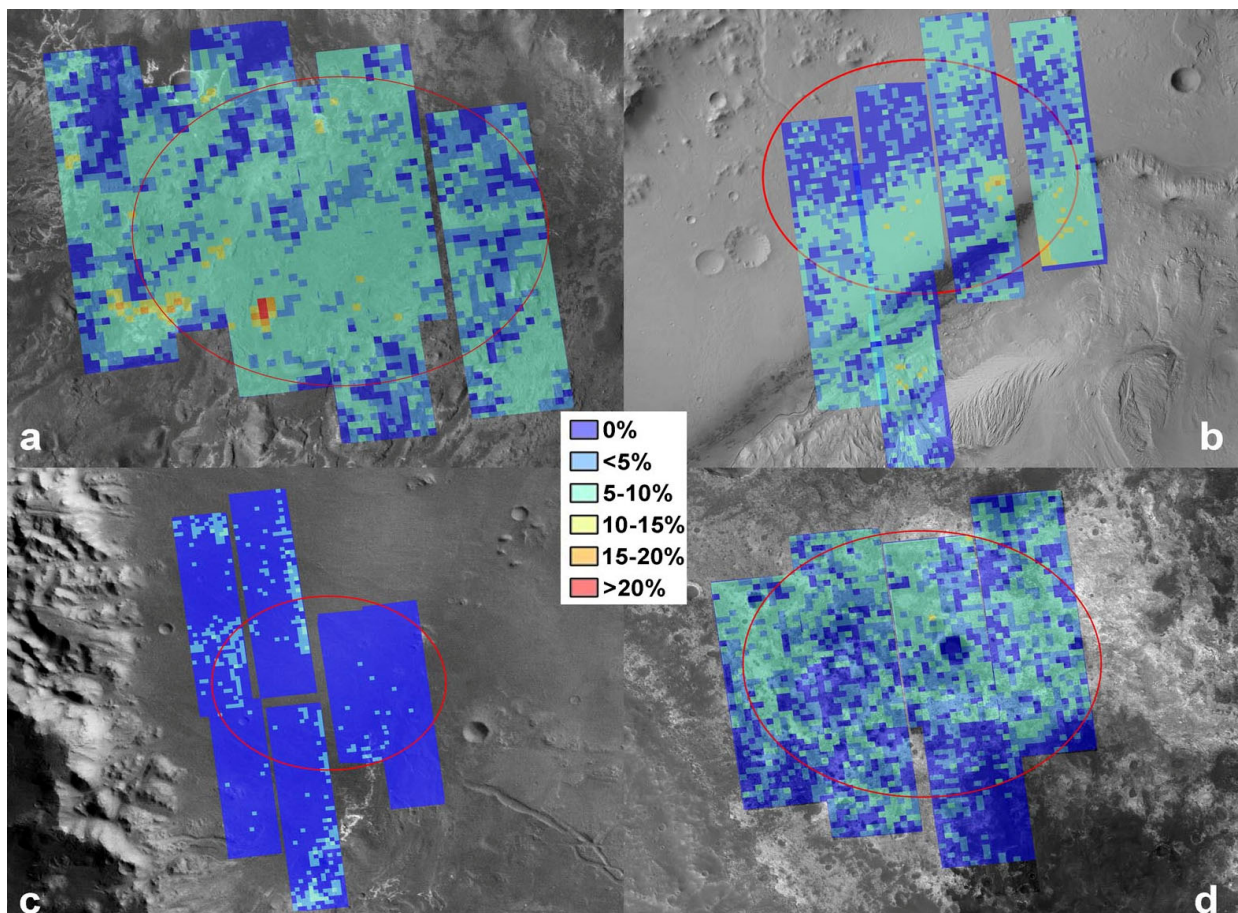

Figure 18. Maps of rock abundance at the final four MSL landing sites: a) Eberswalde, b) Gale, c) Holden, and d) Mawrth derived from rocks measured in HiRISE images in 450 m square bins fit to the model cumulative size-frequency distribution for rocks 1.5-2.25 m diameter with no minimum rock abundance.

Table 3. Number, cumulative fractional area covered by rocks and probability of landing on 1 rock greater than given diameter

Rock Density	Total number of rocks in 150 m tile	Total number of 1.5-2.25 m diameter rocks in 450 m bin	Equivalent cumulative fractional area (%)	Cumulative number of rocks/m² >1.1 m diameter	Probability rover[1] lands on 1 rock> 1.1 m diameter (%)	Cumulative number of rocks/m² >1.2 m diameter	Probability belly pan of rover[2] lands on 1 rock> 1.2 m diameter (%)
High	>100	669 / >321	30 / > 21	0.015	5.93	0.011	2.78
Medium-High	21 – 100	171-320	< 20	0.0081	3.15	0.0054	1.42
Medium-Low	9 – 20	57-170	< 15	0.0047	1.85	0.0031	0.82
Low	4 – 8	4-56	< 10	0.0019	0.75	0.0012	0.31
Very Low	0 – 3	1-3	~ 5	0.000198	0.08	0.0001	0.027

Summary

Substantial improvements to the automated rock detection algorithm have been made beyond those used for the Phoenix landing site selection (Golombek et al. 2008a). These improvements were required to deal with the much more complicated and varied terrain in the MSL landing sites compared with the smooth, flat and uniform albedo northern plains in which Phoenix landed. We used HiRISE images of the Phoenix landing site to accurately extrapolate to surface rock distributions using a hand and automated count on HiRISE images and three surface counts made from lander images. Orbital rock counts follow exponential model size-frequency distributions for 3-4% rock abundance for rocks >0.8 m diameter and surface counts follow model distributions for 2-4% rock abundance for rocks 0.15-0.4 m diameter. Even though measured diameters from orbital and surface data do not overlap, measured distributions follow models within 1% rock abundance and further validate extrapolations of rock abundance using HiRISE images.

Tests using HiRISE images of spacecraft on Mars were used to evaluate five different deconvolution methods to sharpen shadows and improve rock detection accuracy. Best results were found using 4 iterations of blind deconvolution seeded with a Gausian PSF similar to the HiRISE PSF. Deconvolution sharpening allowed measurement of shadows of only 3 pixels (compared with 5 pixels for Phoenix), which allowed measurement of more smaller rocks. We also processed the images in 500x500 pixel tiles to better tune the gamma correction before shadow segmentation (Golombek et al. 2008a). Ellipses are then fit to the shadows, circles are fit to the shadow width at the terminator, and the diameter of the rock and its height are determined from the fit circle diameter, the ellipse length, and the Sun elevation angle.

Steep slopes at some of the landing sites produced shadows that severely skewed the measured cumulative size-frequency distributions. Pilot studies showed that human operators could easily distinguish and remove non-rocks from the image and that the resulting measured size-frequency distributions followed model rock size-frequency distributions for counts over 450 m sided square bins. Because human editing took a long time, an automated fitting routine was developed that fit the number of rocks 1.5-2.25 m diameter to the closest rock abundance model size-frequency distribution. Pilot studies showed good correspondence between hand edited distributions and those determined by the fitting routine.

Maps of the landing sites were produced that show: (1) the total number of rocks in 150 m sided bins, (2) the best fit model rock abundance in 450 m side bins, spaced every 150 m, with rock abundance recorded to the next highest integer rock abundance with a minimum 1 rock per 450 m bin enforced (5% rock abundance), and (3) the best fit model rock abundance in 450 m side bins recorded to the nearest 0.1% rock abundance with bins with no rocks (0% rock abundance). Map (2) was provided to the MSL project for landing simulations. The average number of rocks in 150 m side bins is 13.3, 7.7, 0.3 and 3.7 at Eberswalde, Gale, Holden and Mawrth landing sites, respectively. The average rock abundance derived from map (2) at Eberswalde, Gale, Holden and Mawrth are 6.6±1.9%, 5.8±1.4%, 5.0±0.3% and 5.6±0.9%, respectively. Lower average rock abundances derived from map (3) at Eberswalde, Gale, Holden and Mawrth are 5.4±2.6%, 3.9±3.0%, 0.3±1.1% and 3.3±2.7%, respectively. Average rock abundances of 4-5% for Eberswalde and Gale compare favorably to the rock abundances at the Gusev cratered plains. Landing simulations indicate the probability of failure due to landing on a rock higher than the rover belly pan is 0.30%, 0.17%, 0.03% and 0.08% at Eberswalde, Gale, Holden, and Mawrth landing sites, respectively. Because these probabilities are less than the engineering requirement of a <0.5% chance of landing on a rock taller than the 0.55 m high rover clearance (assumed to be 1.1 m diameter for hemispherical rocks), all sites are safe with respect to rocks and they were not a factor in landing site selection.

References

Arvidson, R. et al. (2008) "Mars Exploration Program 2007 Phoenix landing site selection and characteristics" Journal of Geophysical Research 113, E00A03 http://dx.doi.org/10.1029/2007JE003021

Arvidson, R. E. et al. (2009) "Results from the Mars Phoenix Lander Robotic Arm experiment" Journal of Geophysical Research 114, E00E02 http://dx.doi.org/10.1029/2009JE003408

Biggs, D. S. C., M. Andrews (1997) "Acceleration of iterative image restoration algorithms" Applied Optics 36, 1766-1775.

Bonitz, R. G. et al. (2008) "NASA Mars 2007 Phoenix Lander Robotic Arm and Icy Soil Acquisition Device" Journal of Geophysical Research 113, E00A01 http://dx.doi.org/10.1029/2007JE003030

Brown, W. K., and K. H. Wohletz (1995) "Derivation of the Weibull distribution based on physical principles and its connection to the Rosin-Rammler and lognormal distributions" Journal of Applied Physics 78, 2758–2763.

Christensen, P. R. (1986) "The spatial distribution of rocks on Mars" Icarus 68, 217-238. http://dx.doi.org/10.1016/0019-1035(86)90020-5

Craddock, R. A., M. Golombek, and A. D. Howard (2000) "Analyses of rock size-frequency distributions and morphometry of modified Hawaiian lava flows: Implications for future Martian landing sites" Lunar and Planetary Science XXXI, Abstract #1649, Lunar and Planetary Institute, Houston (CD-ROM).

Garvin, J. B., P. J. Mouginis-Mark and J. W. Head (1981) "Characterization of rock populations on planetary surfaces: Techniques and a preliminary analysis of Mars and Venus" Moon and Planets 24, 355 – 387.

Gilvarry, J. J. (1961) "Fracture of brittle solids I. Distribution function for fragment size in single fracture (theoretical)" Journal of Applied Physics 32, 391–399. http://dx.doi.org/10.1063/1.1736016

Gilvarry, J. J. and B. H. Bergstrom (1961) "Fracture of brittle solids II. Distribution function for fragment size in single fracture (experimental)" Journal of Applied Physics 32, 400– 410. http://dx.doi.org/10.1063/1.1736017

Golombek, M., and D. Rapp (1997) "Size-frequency distributions of rocks on Mars and Earth analog sites: Implications for future landed missions" Journal of Geophysical Research 102, 4117-4129. http://dx.doi.org/10.1029/96JE03319

Golombek, M. P., R. A. Cook, H. J. Moore and T. J. Parker (1997) "Selection of the Mars Pathfinder landing site" Journal of Geophysical Research 102, 3967-3988. http://dx.doi.org/10.1029/96JE03318

Golombek, M. P., H. J. Moore, A. F. C. Haldemann, T. J. Parker and J. T. Schofield (1999) "Assessment of Mars Pathfinder landing site predictions" Journal of Geophysical Research 104, 8585-8594. http://dx.doi.org/10.1029/1998JE900015

Golombek, M. P. et al. (2003a) "Rock size-frequency distributions on Mars and implications for Mars Exploration Rover landing safety and operations" Journal of Geophysical Research 27, 8086 http://dx.doi.org/10.1029/2002JE002035

Golombek, M. P. et al. (2003b) "Selection of the Mars Exploration Rover landing sites" Journal of Geophysical Research 13, 8072 http://dx.doi.org/10.1029/2003JE002074

Golombek, M. P. et al. (2005) "Assessment of Mars Exploration Rover landing site predictions" Nature 436, 44-48. http://dx.doi.org/10.1038/nature03600

Golombek, M. P. et al. (2006) "Geology of the Gusev cratered plains from the Spirit rover transverse" Journal of Geophysical Research 111, E02S07 http://dx.doi.org/10.1029/2005JE002503

Golombek, M. P. et al. (2008a) "Size-frequency distributions of rocks on the northern plains of Mars with special reference to Phoenix landing surfaces" Journal of Geophysical Research 113, E00A09 http://dx.doi.org/10.1029/2007JE003065

Golombek, M. P., A. F. C. Haldemann, R. A. Simpson, R. L. Fergason, N. E. Putzig, R. E. Arvidson, J. F. Bell III and M.T. Mellon (2008b) "Martian surface properties from joint analysis of orbital, Earth-based, and surface observations" Chapter 21 in, The Martian Surface: Composition, Mineralogy and Physical Properties (J. F. Bell III editor) Cambridge University Press, p. 468-497.

Golombek M., et al. (2012) "Selection of the Mars Science Laboratory landing site" Space Science Reviews, http://dx.doi.org/10.1007/s11214-012-9916-y

Gonzalez, R. C. and R. E. Woods (1992) Digital Image Processing, Addison-Wesley Publishing Company, Inc., Reading, MA.

Grant, J. A. et al. (2006) "Distribution of rocks on the Gusev Plains and on Husband Hill, Mars" Geophysical Research Letters 33, L16202 http://dx.doi.org/10.1029/2006GL026964

Hanisch, R. J., R. L. White and R. L. Gilliland (1997) "Deconvolutions of Hubble Space Telescope images and spectra" in Deconvolution of Images and Spectra (P.A. Jansson, editor) 2nd ed., Academic Press, CA.

Hébrard, E., C. Listowski, P. Coll, B. Marticorena, G. Bergametti, A. Määttänen, F. Montmessin, and F. Forget (2012) "An aerodynamic roughness length map derived from extended Martian rock abundance data" Journal of Geophysical Research 117, E04008 http://dx.doi.org/10.1029/2011JE003942

Heet, T. L., R. E. Arvidson, S. C. Cull, M. T. Mellon and K. D. Seelos (2009) "Geomorphic and geologic settings of the Phoenix Lander mission landing site" Journal of Geophysical Research 114, E00E04 http://dx.doi.org/10.1029/2009JE003416

Holmes, T. J., et al. (1995) "Light microscopic images reconstructed by maximum likelihood" in Handbook of Biological Confocal Microscopy (J.B. Pawley, editor) Plenum Press, New York.

Jain, A. K. (1989) Fundamentals of Digital Image Processing, Prentice Hall, NJ.

Kieffer, H. H., T. Z. Martin, A. R. Peterfreund, B. M. Jakosky, E. D. Miner and F. D. Palluconi (1977) "Thermal and albedo mapping of Mars during the Viking primary mission" Journal of Geophysical Research 82(28), 4249-4291. http://dx.doi.org/10.1029/JS082i028p04249

Kirk, R. L. et al. (2008) "Ultrahigh resolution topographic mapping of Mars with MRO HiRISE stereo images: Meter-scale slopes of candidate Phoenix landing

sites" Journal of Geophysical Research 113, E00A24 http://dx.doi.org/10.1029/2007JE003000

McEwen, A. S. et al. (2007a) "Mars Reconnaissance Orbiter's High Resolution Imaging Science Experiment (HiRISE)" Journal of Geophysical Research 112, E05S02 http://dx.doi.org/10.1029/2005JE002605

McEwen, A. S. et al. (2007b) "A Closer Look at Water-Related Geologic Activity on Mars" Science 317, 1706. http://dx.doi.org/10.1126/science.1143987

Moore, H. J. and J. M. Keller (1990) "Surface-material maps of Viking landing sites on Mars" Reports of Planetary Geology and Geophysics Program — 1989, NASA Technical Memorandum 4210, 533–535 (abstract).

Moore, H. J., and J. M. Keller (1991) "Surface-material maps of Viking landing sites on Mars" Reports of Planetary Geology and Geophysics Program — 1990, NASA Technical Memorandum 4300, 160–162 (abstract).

Nowicki, S. A. and Christensen, P. R. (2007) "Rock abundance on Mars from the Thermal Emission Spectrometer" Journal of Geophysical Research 112, E05007 http://dx.doi.org/10.1029/2006JE002798

Rosin, P. and E. Rammler (1933) "The laws governing the fineness of powdered coal" Journal of the Institute of Fuel 7, 29-36.

Sizemore, H. G., M. T. Mellon and M. P. Golombek (2009) "Ice table depth variability near small rocks at the Phoenix landing site, Mars: A pre-landing assessment" Icarus 199, 303-309. http://dx.doi.org/10.1016/j.icarus.2008.10.008

Sizemore, H. G., M. T. Mellon, M. L. Searls, M. T. Lemmon, A. P. Zent, T. L. Heet, R. E. Arvidson, D. L. Blaney and H. U. Keller (2010) "In situ analysis of ice table depth variations in the vicinity of small rocks at the Phoenix landing site" Journal of Geophysical Research 115, E00E09 http://dx.doi.org/10.1029/2009JE003414

Spencer, D. A., D. S. Adams, E. Bonfiglio, M. Golombek, R. Arvidson and K. Seelos (2009) "Phoenix landing site hazard assessment and selection" Journal of Spacecraft and Rockets 46, 1196-1201. http://dx.doi.org/10.2514/1.43932

Ward, J. G. et al. (2005) "The size-frequency and areal distribution of rock clasts at the Spirit landing site, Gusev Crater, Mars" Geophysical Research Letters 32, L11203 http://dx.doi.org/10.1029/2005GL022705

Wohletz, K. H., M. F. Sheridan and W. K. Brown (1989) "Particle size distributions and the sequential fragmentation/transport theory applied to volcanic ash" Journal of Geophysical Research 94, 15,703–15,721. http://dx.doi.org/10.1029/JB094iB11p15703

Yingst, R. A., A. F. C. Haldemann, K. L. Biedermann and A. M. Monhead (2007) "Quantitative morphology of rocks at the Mars Pathfinder landing site" Journal of Geophysical Research 112, E06002 http://dx.doi.org/10.1029/2005JE002582

Yingst, R. A., L. Crumpler, W. H. Farrand, R. Li and P. de Souza (2010) "Constraints on the geologic history of 'Home Plate' materials provided by clast morphology and texture" Journal of Geophysical Research 115, E00F13 http://dx.doi.org/10.1029/2010JE003668